energies

MDPI

Article

Degradation-Aware Power Allocation and Power-Matching Control in an Off-Grid Wind–Hydrogen System

Dongdong Li, Xin Lv, Fan Yang * and Yifan Deng

College of Electrical Engineering, Shanghai University of Electric Power, Shanghai 200090, China
* Correspondence: smartgridcontrol@163.com

Abstract

Wind power-to-hydrogen has emerged as an important pathway for the large-scale utilization of renewable energy. However, the inherent intermittency and randomness of wind power pose significant challenges to power balance and stable operation in off-grid wind–hydrogen systems. To address these issues, this paper investigates coordinated control strategies for an off-grid wind-powered hydrogen production system. On the wind turbine side, a rotor-speed droop control strategy based on wind speed input is proposed to regulate the turbine power output and mitigate power fluctuations caused by wind variations. On the electrolyzer side, a degradation-aware power allocation strategy is developed for multiple proton exchange membrane water electrolyzers (PEMWE), considering their voltage degradation characteristics under different operating conditions. The simulation results demonstrate that the proposed strategy effectively enhances system performance and operational stability under off-grid conditions. The overall system efficiency is improved by 5%, while the RMS deviation of the DC bus voltage is reduced by 17.31%, indicating improved power balance and smoother operation of the off-grid wind–hydrogen system.

Keywords: off-grid hydrogen production; PEM water electrolyzer; wind turbine control; power allocation; degradation modeling

1. Introduction

With the increasing prominence of energy shortages, environmental pollution, and climate change issues, the large-scale development of renewable energy has become of great significance. Renewable power generation, particularly wind power, is inherently stochastic and intermittent. When directly integrated into the power grid, such characteristics may induce voltage fluctuations, frequency deviations, and other power quality issues, potentially threatening the secure and stable operation of the grid [1–3]. To ensure the safe and economical operation of power systems with a high penetration of renewable energy, effective coordination between renewable energy sources and energy storage systems is essential. Hydrogen energy storage, which exploits the mutual convertibility between electrical energy and hydrogen energy, has emerged as a large-scale energy storage solution and is widely regarded as one of the key technologies for addressing energy crises and enhancing renewable energy utilization [4–6].

In this context, off-grid wind–solar hydrogen production systems have been recognized as an effective solution for promoting renewable energy consumption and optimizing the energy structure [7,8]. Such systems not only improve the utilization efficiency of wind and solar resources through local consumption, but also provide a practical pathway for exploring the emerging energy strategy of green hydrogen [9]. Under off-grid operating

Check for updates

Academic Editor: Adrian Ilinca

Received: 28 February 2026
Revised: 29 March 2026
Accepted: 30 March 2026
Published: 1 April 2026

Copyright: © 2026 by the authors. Licensee MDPI, Basel, Switzerland. This article is an open access article distributed under the terms and conditions of the Creative Commons Attribution (CC BY) license.

conditions, the strong power fluctuations in renewable sources impose more stringent requirements on hydrogen production systems. Proton exchange membrane water electrolysis (PEMWE), characterized by a fast dynamic response, compact structure, and direct coupling capabilities with renewable power sources, has demonstrated strong competitiveness in renewable-energy-based hydrogen production systems [10,11]. However, in off-grid wind-powered hydrogen production systems, the stable operation and overall lifetime of the system largely depend on the power coordination between wind power generation and hydrogen production loads. Due to the inherent intermittency and stochastic nature of wind energy, the output power of wind turbines fluctuates significantly, while electrolyzers operate under strict power constraints, including the minimum start-up power and preferred operating power ranges [12,13]. Therefore, maintaining power balance on the generation side and achieving rational power allocation on the electrolyzer side become two key challenges for ensuring the stability and reliability of off-grid wind–hydrogen systems. To address these issues, coordinated control strategies are required to mitigate wind-induced power fluctuations while enabling the efficient utilization of electrolyzers and accounting for their degradation characteristics [14–16].

To address the power fluctuation and coordination issues in renewable-powered hydrogen production systems, extensive research efforts have been conducted. Existing studies mainly focus on mitigating renewable power fluctuations and improving the coordination between power generation and hydrogen production loads. Various approaches have been proposed, including the integration of energy storage devices such as supercapacitors to buffer wind power variations, the development of coordinated control strategies based on DC bus architectures, and the establishment of electromagnetic transient models to analyze the dynamic interaction between renewable sources and hydrogen production systems [8,17,18]. These studies demonstrate that coordinated control and auxiliary energy storage can effectively enhance the operational stability of wind–hydrogen systems under fluctuating renewable conditions.

In addition to system-level coordination, increasing attention has been devoted to optimizing power allocation strategies for electrolytic hydrogen production systems. Several studies have proposed control and scheduling methods to regulate the operating states of multiple hydrogen production units, including queue-based start–stop management algorithms, predictive power matching strategies considering electrolyzer operating constraints, and efficiency-oriented optimal scheduling approaches for electrolyzer arrays [19–21]. Although these studies improve renewable energy utilization and system performance, most existing research focuses primarily on alkaline electrolyzers, while the impacts of renewable power fluctuations and frequent start–stop operations on electrolyzer lifetime remain insufficiently investigated.

Motivated by these challenges, this paper proposes a wind turbine-side rotor droop control strategy based on wind speed input to enhance the operational stability of off-grid wind-powered hydrogen production systems under power fluctuations. Furthermore, on the electrolyzer-side power allocation module, the voltage degradation rates under different operating conditions are employed to quantify the degradation behavior of PEMWE, and a voltage-degradation-aware power allocation strategy for off-grid wind–solar hydrogen production systems is developed.The main contributions of this work are as follows:

1. For the off-grid wind-to-hydrogen system, a dual-side coordinated control strategy is proposed. By integrating rotor speed droop control and pitch angle-based aerodynamic torque control on the wind turbine side with DC bus power smoothing control, the strategy achieves real-time power matching while exhibiting enhanced disturbance rejection capabilities. Under noisy wind speed conditions, the RMS deviation of the DC bus voltage is reduced by 17.31%.

2. A degradation-aware power allocation strategy is proposed, which coordinates the operating power of multiple PEMWE stacks according to their individual degradation characteristics. This effectively mitigates uneven degradation among stacks, reduces start–stop operations compared with the average allocation strategy, and improves the efficiency by approximately 5% compared with a sequential (stepwise) power allocation approach.

The remainder of this paper is organized as follows. Section 2 describes the architecture of the considered wind–hydrogen coupled system and develops the electrochemical model and voltage degradation model of the PEMWE. Section 3 presents the coordinated control strategy for maintaining power balance between the wind generation side and the hydrogen production load. Section 4 proposes a power allocation strategy for electrolyzers considering operational constraints and degradation characteristics. Simulation results and performance evaluations are provided in Section 5 to verify the effectiveness of the proposed methods. Finally, the conclusions are summarized in Section 6.

2. Framework and Modeling of the Off-Grid Wind–Hydrogen Integrated System

As shown in Figure 1, the wind-to-hydrogen system studied in this work mainly consists of several key components: a PMSG wind turbine, a machine-side AC/DC converter, a Buck-type DC/DC converter, and a PEMWE. For simplicity of analysis, it is assumed that the horizontal-axis wind turbine is directly coupled with the rotor of the PMSG, and the generator adopts a symmetrical salient-pole structure.

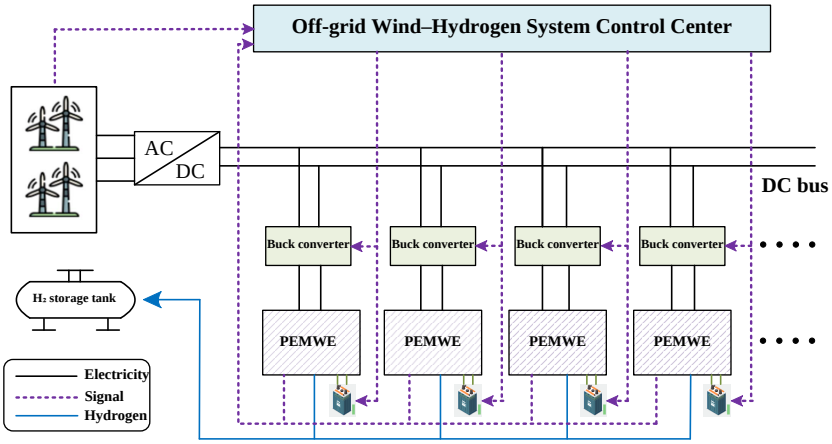


Figure 1. Structural diagram of off-grid wind–hydrogen production system.

Multi-stack electrolyzer arrays in engineering applications are typically connected in series, parallel, or hybrid series–parallel and cascaded configurations. Different topologies exhibit distinct characteristics in terms of control flexibility, system reliability, and cost, and therefore directly influence the implementation of power dispatch strategies and overall system performance.

In a series configuration, individual stacks are connected sequentially to form a unified circuit, where the system current is identical while the voltages are accumulated. Although this structure is relatively simple, the strong electrical coupling among stacks makes the independent regulation of each stack difficult. Moreover, the failure or performance degradation of a single stack may affect the operation of the entire system, which limits system reliability. As a result, this topology is not suitable for multi-stack operation scenarios requiring dynamic power redistribution.

In contrast, the parallel configuration equips each stack with an independent power conversion unit, allowing all stacks to share the same DC bus voltage while their currents can be regulated individually. This enables stack-level independent control and differentiated load allocation, thereby improving operational flexibility. However, since each stack requires a dedicated converter and control unit, the hardware cost and control complexity are relatively higher.

Hybrid series–parallel and cascaded configurations provide a compromise between cost and control performance. Nevertheless, due to the structural coupling among stacks, fully independent power regulation is still difficult to achieve. Considering that this study focuses on a degradation-aware power allocation strategy, which requires independent regulation and dynamic redistribution of the input power of each stack, a parallel architecture is adopted in this work. Although this structure increases the number of DC–DC converters and thus the system cost and complexity, its modular characteristics enhance system fault tolerance and scalability while enabling stack-level power regulation, which helps mitigate uneven degradation and extend the overall system lifetime.

PEMWEs cannot be immediately restarted after a complete shutdown. To prevent frequent start–stop cycles that may lead to hydrogen accumulation at the anode and crossover through the membrane to the cathode, potentially causing safety issues, some studies have recommended using a low-power external supply to maintain stack voltage when no input power is available [14,15]. In this work, each 500 kW PEMWE stack is supplied with a 5 kW low-power external source to maintain its minimum operating voltage, thereby reducing the risk of frequent shutdowns.

2.1. Electrochemical Model of the PEMWE

The electrochemical model of the PEMWE forms the core of the overall model. Terminal voltage of the PEMWE cell u_{el} is the sum of open-circuit reversible voltage u_{ocv}, activation overpotential η_{act}, and ohmic polarization overpotential η_{ohm} [22].

$$u_{\mathrm{el}} = u_{\mathrm{ocv}} + \eta_{\mathrm{act}} + \eta_{\mathrm{ohm}} \tag{1}$$

The open-circuit reversible voltage u_{ocv} can be derived from the Nernst equation as follows:

$$\begin{cases} u_{\mathrm{ocv}} = u_{\mathrm{rev}} + R_0 \dfrac{T}{2F} \ln\left(\dfrac{P_{\mathrm{H_2}} \sqrt{P_{\mathrm{O_2}}}}{a_{\mathrm{H_2O}}} \right) \\ u_{\mathrm{rev}} = 1.229 - 0.0009(T - 298) \end{cases} \tag{2}$$

where R_0 is the gas constant. T represents the reaction temperature in the cell. F is the Faraday constant. $P_{\mathrm{H_2}}$ is the partial pressure of oxygen at the anode and $a_{\mathrm{H_2O}}$ is the water activity.

The η_{act} refers to the loss of electromotive force in electrochemical reactions, primarily influenced by temperature, catalysts, and electrodes. It is represented by the electrochemical reaction dynamic equation as follows:

$$\begin{cases} \eta_{\mathrm{act}} = \eta_{\mathrm{act},a} + \eta_{\mathrm{act},c} \\ \eta_{\mathrm{act},a} = \dfrac{R_0 T}{\alpha_a F} \operatorname{arcsinh}\left(\dfrac{i}{2 i_{o.a}} \right) \\ \eta_{\mathrm{act},c} = \dfrac{R_0 T}{\alpha_c F} \operatorname{arcsinh}\left(\dfrac{i}{2 i_{o.c}} \right) \end{cases} \tag{3}$$

where $\eta_{\mathrm{act},a}$ and $\eta_{\mathrm{act},c}$ denote the activation overpotentials at the anode and cathode, respectively, representing the electrochemical kinetic losses associated with the water-splitting

reactions at each electrode. α_a and α_c are the respective charge transfer coefficients, $i_{o.a}$ and $i_{o.c}$ are the corresponding exchange current densities. i is the operating current density.

The PEMWE exhibits resistance to both electron and proton transport, with the protonic resistance typically being about ten times greater than the electronic one. This resistance is usually represented as an equivalent ohmic term. Accordingly, the ohmic polarization overpotential η_{ohm} can be expressed according to Ohm's law as follows:

$$\begin{cases} \eta_{\text{ohm}} = R_{\text{mem}}\, i \\ i = \dfrac{I_{\text{el}}}{A} \\ R_{\text{mem}} = \dfrac{\delta_{\text{mem}}}{\sigma_{\text{mem}}} \\ \sigma_{\text{mem}} = (0.5139\lambda_0 - 0.326)\exp\left[1268\left(\dfrac{1}{303} - \dfrac{1}{T}\right)\right] \end{cases} \tag{4}$$

where R_{mem} is the equivalent membrane resistance. I_{el} represents the electrolyzer current. A is the effective area of the electrolyzer. δ_{mem} and σ_{mem} are the thickness and conductivity of the membrane, respectively. λ_0 denotes the membrane water content.

Based on Equations (1)–(4), the polarization curves of the PEMWE at different temperatures are obtained in MATLAB/Simulink (R2024a, The MathWorks, Inc., Natick, MA, USA), as shown in Figure 2. The results are consistent with those reported by Mao [10], where the equivalent parameters of a PEM electrolyzer engineering model were identified.

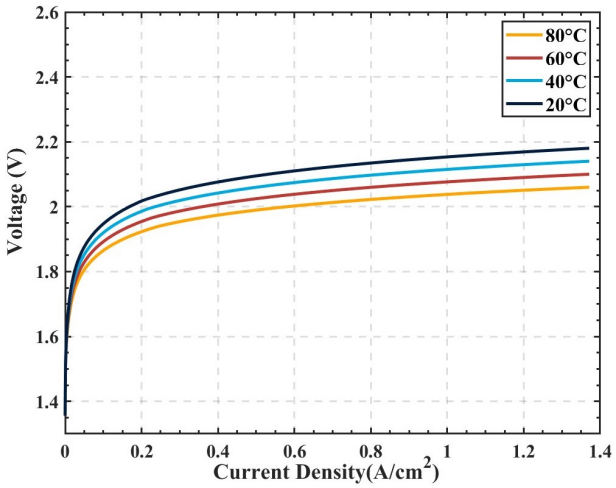


Figure 2. Polarization curves of PEM electrolyzer at different temperatures.

The efficiency of an electrolyzer can be expressed as the product of the current efficiency and the voltage efficiency. Among these, the voltage efficiency reflects the internal electrical energy utilization of the electrolyzer and can be defined as the ratio of the theoretical electrolysis voltage of water to the actual operating voltage. The theoretical electrolysis voltage of water can be represented by the thermoneutral voltage.

The thermoneutral voltage characterizes the enthalpy change of the water electrolysis process, including both the Gibbs free energy change and the entropy change of the reaction. When no external heat supply is provided and water is decomposed solely by electrical energy, the required thermoneutral voltage is 1.48 V. Under this condition, the voltage efficiency can be expressed as

$$\eta_{\text{v}} = \frac{u_{\text{tn}}}{u_{\text{el}}} \times 100\% \tag{5}$$

where u_{tn} denotes the thermoneutral voltage and u_{el} represents the actual electrolyzer operating voltage.

The current efficiency, also known as the Faradaic efficiency, can be expressed as a function of the current density according to the following empirical relationship:

$$\eta_{\mathrm{F}} = \frac{j^2}{f_1 + j^2} f_2 \tag{6}$$

where η_{F} denotes the current efficiency, j is the current density, and f_1 and f_2 are Faradaic-related empirical parameters.

Accordingly, the overall efficiency of the electrolyzer can be expressed as the product of the voltage efficiency and the Faradaic efficiency:

$$\eta = \eta_{\mathrm{v}}\, \eta_{\mathrm{F}} \tag{7}$$

2.2. Lifetime Degradation Model of PEMWE

In practical operation, the lifetime degradation of electrolyzers is influenced by multiple factors, such as temperature, humidity, water flow variation, and membrane–electrode assembly (MEA) aging. However, accurately modeling all these mechanisms simultaneously remains challenging. Therefore, degradation in this study is characterized through stack voltage variation under different power operating conditions, which is closely related to the operating power and its fluctuations under given conditions. Factors such as temperature dynamics, humidity effects, and detailed MEA aging mechanisms are not explicitly considered in the present model.

The voltage degradation rate of PEMWEs varies under different operating conditions. Low and medium constant input power levels have a limited impact on the voltage degradation rate, whereas frequent start–stop events and high constant input power significantly accelerate voltage degradation, with degradation rates reaching up to 230 mV/h. In addition, fluctuating operation within the rated power range of the PEMWE can mitigate aging in the short term; however, the opposite effect is observed over long-term operation. More critically, high-power fluctuation operation leads to severe voltage degradation.

P_t denotes the turning power point at which the voltage degradation rate is relatively low, and P_{el} represents the rated power of the electrolyzer. The power ranges under five operating conditions and the corresponding voltage degradation rates of a single PEMWE cell are shown in Table 1. According to [23], the voltage degradation behavior of PEMWE under different operating conditions allows for the classification of operation into five categories: maintenance operation, low-power fluctuating operation, constant rated power operation, and high-power fluctuating operation. The power used for the maintenance operation is set based on the experimental data reported in [23], corresponding to approximately 1% of the rated power of a single electrolyzer stack. In this work, the turning power point P_t of the 500 kW single-stack PEMWE is set to 350 kW, corresponding to a high-power operating current density of 2 A/cm^2.

Table 1. Power range and PEMWE single-cell voltage degradation rate for five operating conditions.

Operating Conditions	Symbol	Range (KW)	Degradation
Maintaining operation	V_m	5	1.5 μV/h
Low power fluctuation operation	V_{fl}	$(5, P_t)$	50 μV/h
Constant turning power operation	V_{ct}	P_t	20 μV/h
High power fluctuation operation	V_{fh}	(P_t, P_{el})	66 μV/h
Constant rated power operation	V_{cr}	P_{el}	196 μV/h

The total degradation of the i-th PEMWE stack during one scheduling cycle is expressed as the sum of the degradation contributions under different operating states, i.e.,

$$D(i) = D_1(i) + D_2(i) + D_3(i) + D_4(i) + D_5(i) \tag{8}$$

where the degradation components corresponding to the five operating conditions are defined as

$$\begin{cases} D_1(i) = n_{\text{el}}\, V_m\, t_m(i) \\ D_2(i) = n_{\text{el}}\, V_{fl}\, t_{fl}(i) \\ D_3(i) = n_{\text{el}}\, V_{ct}\, t_{ct}(i) \\ D_4(i) = n_{\text{el}}\, V_{fh}\, t_{fh}(i) \\ D_5(i) = n_{\text{el}}\, V_{cr}\, t_{cr}(i) \end{cases} \tag{9}$$

where $D(i)$ denotes the total voltage degradation of the i-th PEMWE stack within one scheduling cycle, and $D_k(i)$ represents the degradation contribution under operating condition k.

V_m, V_{fl}, V_{ct}, V_{fh}, and V_{cr} denote the voltage degradation rates corresponding to maintaining operation, low power fluctuation operation, constant turning power operation, high power fluctuation operation, and constant rated power operation, respectively, as listed in Table 1. $t_m(i)$, $t_{fl}(i)$, $t_{ct}(i)$, $t_{fh}(i)$, and $t_{cr}(i)$ represent the cumulative operating durations of the i-th stack under the corresponding operating conditions. n_{el} is the number of cells in a PEMWE stack.

For a PEM electrolyzer array consisting of n stacks, the overall degradation level is evaluated by the average degradation of all stacks, which can be written as

$$D = \frac{1}{n} \sum_{i=1}^{n} D(i) \tag{10}$$

Based on the above analysis, Figure 3 illustrates the efficiency variation of a single-stack PEMWE with a rated power of 16 kW under different input power conditions. When different levels of voltage degradation are considered, the efficiency curves shift downward overall, and the efficiency decline becomes more pronounced at higher power levels. This observation is consistent with the accelerated stress test (AST) results on performance degradation reported by Weiss [14].

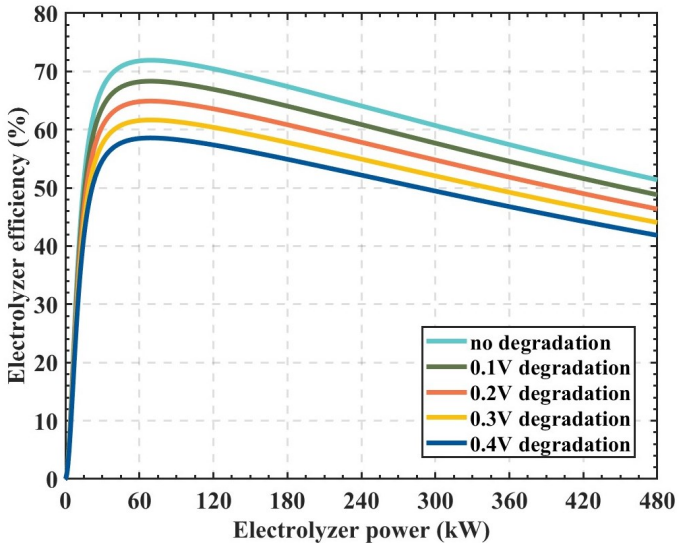


Figure 3. Electrolyzer efficiency–power characteristics considering voltage degradation.

3. Dynamic Power Coordination Control

3.1. Rotor Speed Droop Control

Figure 4 presents the control block diagram of the machine-side converter for the proposed off-grid wind turbine. In this diagram, the current inner loop uses a rotor flux-oriented vector control method, where the reference value of the stator current's d-axis component is set to 0. The control of the electromagnetic torque of the synchronous generator is achieved by adjusting the q-axis component of the stator current, enabling precise tracking of the mechanical angular velocity.

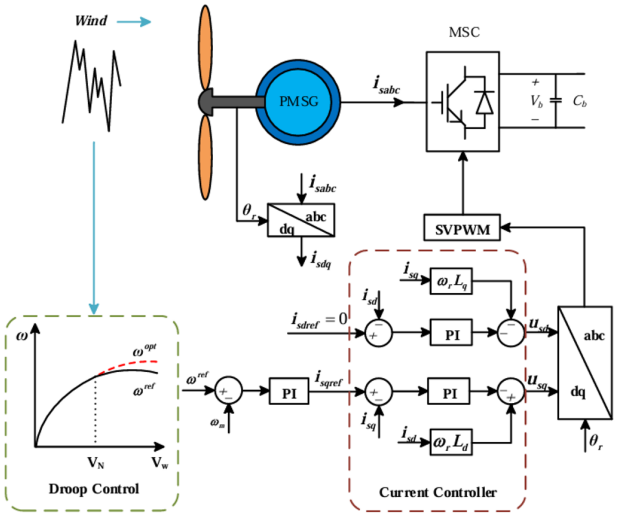


Figure 4. Control diagram of the machine-side converter.

Due to the close relationship between the optimal output power P_{opt} of the wind turbine at different wind speeds and the corresponding ω_{opt}, controlling ω_m to adjust the power output of the wind turbine is a fast-response and flexible approach . However, under off-grid, no-storage operating conditions, excessive adjustment of the rotational speed can lead to a significant increase or decrease in torque, causing instability or leading to insufficient power from the motor. Therefore, controlling the rotor speed of the wind turbine is considered a power control measure with fast response to wind speed variations.

As shown in the figure, through a PI-based speed controller, ω_m follows the reference value ω_{Ref}, and the dynamic wind speed–rotor speed droop control is applied in the outer loop. According to the curve $V_w - \omega_{\text{opt}}$ of the wind turbine, when $V_w < V_N$, the speed of the wind turbine is maintained at ω_{opt}, maximizing the utilization of the wind energy. When $V_w > V_N$, the system applies droop control to the rotor speed based on wind speed variations.The specific control law is as follows:

$$\omega_{\text{ref}} = \begin{cases} \omega_{\text{opt}}, & V_{\min} < V \le V_N \\ \omega_{\text{opt}} - r(V - V_N), & V_N < V \le V_{\max} \end{cases} \tag{11}$$

The droop coefficient is given by $r = \frac{\Delta\omega_{\max}}{V_{\max} - V_N}$, where $\Delta\omega_{\max}$ is the maximum value of the speed adjustment within the safe operating range of the wind turbine.

3.2. Pitch Angle Control

In the energy conversion process of a wind turbine system, wind energy is first captured aerodynamically by the blades, then transmitted through the main shaft and drivetrain to the generator side, and finally delivered to the DC bus or grid via power

electronic converters. Essentially, this process constitutes a multi-physics coupled dynamic system involving aerodynamic, mechanical, and electromagnetic subsystems.

If only the generator-side electromagnetic power or electromagnetic torque is taken as the input variable for modeling and control, the resulting response inherently includes the effects of drivetrain efficiency, shaft damping and elasticity, as well as electrical losses in the generator. Consequently, it becomes difficult to accurately reflect the direct impact of wind speed disturbances on blade aerodynamic loading. Under highly stochastic wind conditions, electromagnetic variables often exhibit amplitude attenuation and dynamic lag, which reduces the sensitivity of the system to variations in the original wind energy input.

To address this issue, an aerodynamic torque and speed observation mechanism is introduced in this section for state reconstruction, thereby improving modeling accuracy and control performance. Based on the mechanical dynamics of the wind turbine drivetrain, an aerodynamic torque observer is constructed and embedded into the pitch angle control loop, as illustrated in Figure 5.

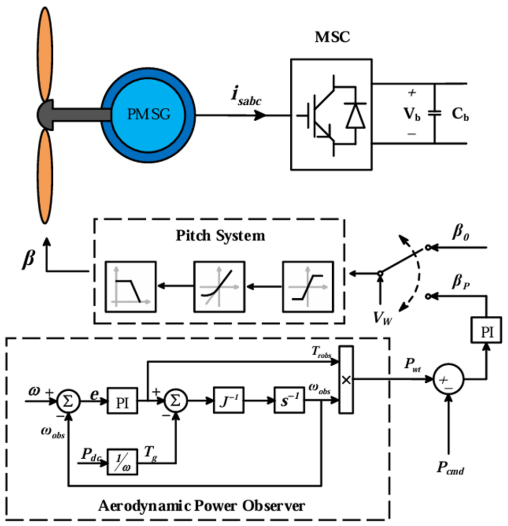


Figure 5. Control diagram of the pitch angle.

The general torque balance equation of the rotating system is expressed as

$$J\frac{d\omega_r}{dt} = T_a - T_e - T_d \tag{12}$$

In the wind energy conversion system, the driving torque corresponds to the aerodynamic torque T_a, while the resisting torque T_d is mainly caused by viscous damping in the shaft system. It can be approximated as a linear damping term proportional to the rotational speed:

$$T_d = B\omega_r \tag{13}$$

Accordingly, the equivalent rotational dynamic equation of the wind turbine–generator system can be written as

$$J\frac{d\omega_r}{dt} = T_a - T_e - B\omega_r \tag{14}$$

Rearranging yields the following aerodynamic torque expression:

$$T_a = J\frac{d\omega_r}{dt} + T_e + B\omega_r \tag{15}$$

It can be observed that the aerodynamic torque is fundamentally determined by the rotor inertia term, the electromagnetic torque, and the damping component. Therefore,

once the rotor speed dynamics and electromagnetic torque information are available, the aerodynamic torque can be reconstructed without direct wind speed measurement.

In practical operation, wind speed is stochastic and uncertain, and wind speed measurements inherently contain delay and error. Directly using wind speed to construct control variables would degrade system dynamic performance and robustness. In this work, the aerodynamic torque is treated as an unknown input, and a torque-imbalance estimation is constructed based on the closed-loop speed error to achieve online reconstruction of the aerodynamic input.

The rotor speed error is first defined as

$$e_\omega = \omega_{ref} - \omega_r \tag{16}$$

The error signal is processed by a PI controller to generate an intermediate variable

$$u = K_p e_\omega + K_i \int e_\omega dt \tag{17}$$

When aerodynamic torque disturbances occur, the rotor speed deviates from its reference value, and the PI controller adjusts the electromagnetic torque command to restore speed tracking. Under small-signal and closed-loop stable conditions, the PI output can be approximated as

$$u \approx J\frac{d\omega_r}{dt} \tag{18}$$

Thus, the estimated aerodynamic torque can be constructed as

$$T_{a,obs} = u + T_e + B\omega_r \tag{19}$$

where T_e is the known electromagnetic torque, introduced for compensation. By incorporating the electromagnetic and damping components, an equivalent reconstruction of the actual aerodynamic torque is achieved.

The aerodynamic torque observer therefore acts as an equivalent disturbance reconstruction module derived from the mechanical dynamic equilibrium, enabling the real-time estimation of aerodynamic input for subsequent power regulation.

Accordingly, in the modeling and control design of the off-grid wind-to-hydrogen system shown in Figure 5, the aerodynamic torque and rotor speed observation values (denoted with the subscript "obs") are adopted as key state variables.

Before the wind speed reaches the rated region, the turbine operates in maximum power tracking mode, and the pitch angle is maintained at its initial setting (typically 0°) to ensure optimal aerodynamic efficiency.

When the wind speed exceeds the rated wind speed v_{rated}, the system enters the power-limited operating region. The deviation between the actual turbine output power P_w and the reference power limit P_{lim} is defined as

$$e_P = P_{lim} - P_w \tag{20}$$

The power deviation is processed by a PI controller to generate the pitch angle reference:

$$\beta_{ref} = K_{p\beta} e_P + K_{i\beta} \int e_P dt \tag{21}$$

The resulting pitch command is further subjected to rate and amplitude constraints to ensure bounded and physically feasible actuation.

Since pitch angle control relies on mechanical systems to adjust the blade angle, it may not respond quickly enough during rapid wind speed fluctuations. Therefore, it is combined with the rotor speed control mentioned above to achieve power stability.

This study adopts a hierarchical multi-timescale modeling framework to coordinate the fast dynamics of the wind turbine and the slow dynamics of the electrolyzer power allocation, as shown in Figure 6. Specifically, the wind turbine control is implemented at a sub-second timescale to regulate rotor speed and output power under stochastic wind speed variations, while the power allocation among multiple electrolyzers is performed at an hourly timescale based on available wind power and operational constraints.

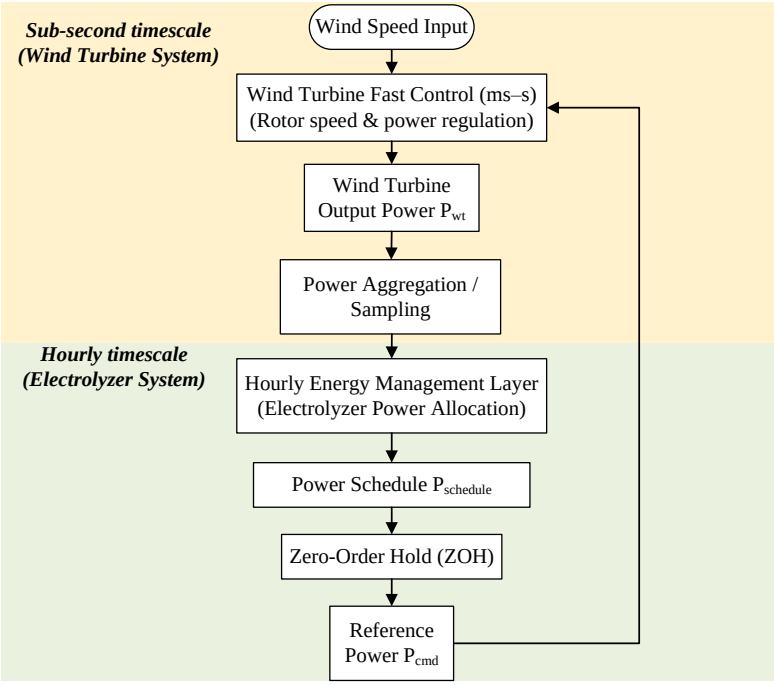


Figure 6. Multi-timescale coordination framework of the wind-to-hydrogen system, including fast wind turbine control and slow electrolyzer power allocation with ZOH-based coupling.

To bridge the two timescales, a zero-order hold (ZOH) mechanism is introduced. The hourly scheduling layer generates a piecewise constant power reference P_{schedule}, which is held constant within each scheduling interval and provided to the wind turbine control layer as the reference signal P_{cmd}. The wind turbine controller then tracks this reference in real time through pitch angle control and generator-side control.

3.3. DC Bus Voltage Control

Control of the machine side can meet the system's power requirements under steady-state conditions. However, when there are sudden changes in wind speed, the variation in wind speed directly affects the wind turbine's output power, leading to a decrease in mechanical power. The reduction in mechanical power causes a decrease in the input current to the machine-side converter, which in turn affects the voltage control and power balance on the machine side [24–26].

As shown in Figure 7, the PEMWE is connected to the DC bus via a buck-type DC/DC converter. Considering the bus voltage fluctuations during the operation of the off-grid wind hydrogen production system, The buck DC/DC converter is used to regulate and optimize the dynamic distribution of energy, maintaining the bus voltage at the system's normal operating point V_{base}.

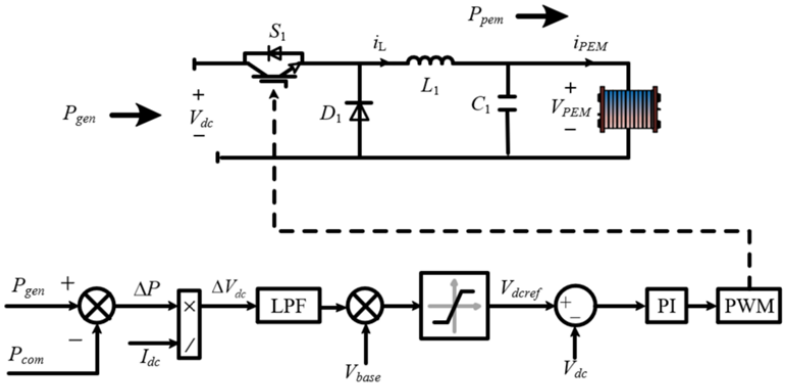


Figure 7. Control the DC bus voltage through a buck DC/DC converter.

In the proposed system, the dc-link voltage reference V_{dc}^{ref} is obtained by adding a power-smoothing index ΔV_{dc}^{*} to the rated dc-link voltage V_{base}. The smoothing index is derived from the output power fluctuations of the PMSG. Let the smoothed power be P_{com}, the actual generator-side converter output power be P_{gen}, and the charge/discharge power of the dc-link capacitor be ΔP_{dc}. The charge/discharge power ΔP_{dc} is expressed as

$$\Delta P_{dc} = V_{dc} C \frac{dV_{dc}}{dt} = P_{\text{com}} - P_{\text{gen}}, \tag{22}$$

where the smoothing command P_{com} is obtained by passing P_{gen} through a low-pass filter. Using the dc-link current I_{dc}, the smoothing index ΔV_{dc} is calculated as

$$\Delta V_{dc} = \frac{\Delta P_{dc}}{I_{dc}}. \tag{23}$$

The low-pass filtering of ΔV_{dc} removes high-frequency fluctuations and contributes to a smoother power delivery within the system. In this study, a first-order low-pass filter (LPF) is employed, with the transfer function

$$G_{\text{LPF}}(s) = \frac{1}{\tau s + 1}$$

where the time constant is set to $\tau = 0.5$ s, corresponding to a cutoff frequency of approximately 0.32 Hz. This cutoff frequency is selected based on the characteristic time scales of wind power fluctuations, allowing high-frequency noise to be effectively attenuated while preserving the low-frequency power variations relevant to DC bus voltage regulation and electrolyzer power matching. Using a representative two-step disturbance as an example, as shown in Figure 8, this configuration effectively suppresses high-frequency variations such as wind speed noise and measurement jitter, while preserving the low-frequency power dynamics that influence energy balance.

The DC-link capacitance also has a significant influence on the dynamic performance and stability of the system. A relatively small capacitance reduces the energy buffering capability of the DC bus, making the bus voltage more sensitive to wind-induced power fluctuations and thereby increasing the electrical stress on the DC/DC converter and the PEM electrolyzer. Conversely, an excessively large capacitance can effectively suppress voltage fluctuations and enhance system stability, but at the expense of slower DC-link voltage dynamics, as well as increased system volume and cost.

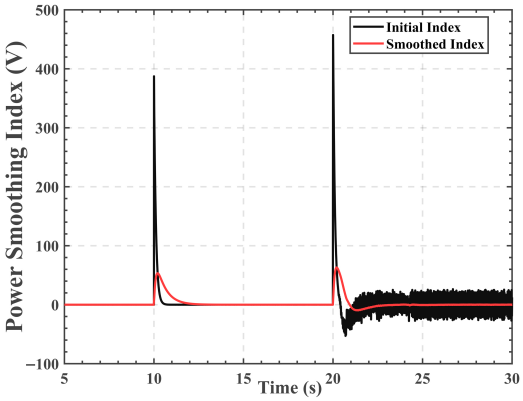


Figure 8. Effect of the low-pass filter on power disturbance smoothing.

To verify the closed-loop stability of the proposed DC bus voltage control strategy at a representative operating point, a frequency-domain stability analysis is conducted under standard small-signal modeling assumptions. The duty-cycle–to–output-voltage small-signal open-loop transfer function of a single-phase Buck converter interfaced with the PEM electrolyzer is analytically derived. Based on this model, the open-loop Bode characteristics of the DC bus voltage control loop at the representative operating conditions are analyzed to evaluate the phase margin and gain margin, thereby providing a quantitative verification of the local closed-loop stability and stability margins of the proposed control strategy.

As shown in Figure 9, the PEM electrolyzer is modeled as a second-order RC circuit to capture its voltage distribution and dynamic behavior. Here, V_{rev} is the fundamental electrolysis voltage, R_{ohm} accounts for membrane and electrode resistance, and C_1 and C_2 are the cathode and anode equivalent capacitances from double-layer effects.

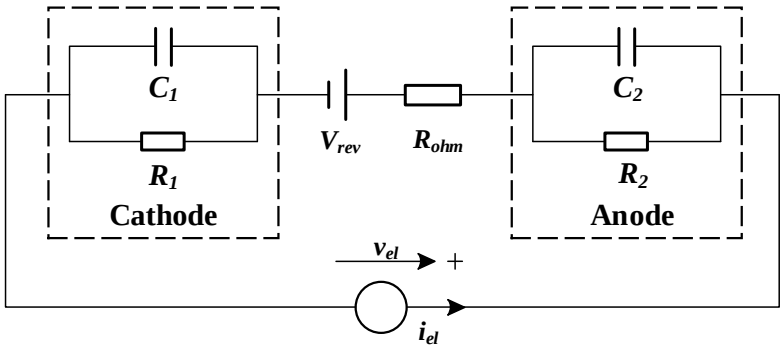


Figure 9. A equivalent circuit model for PEM electrolyzers.

The equivalent circuit of the converter and electrolyzer within one switching period is shown in Figure 10, corresponding to state 1 and state 2, respectively.

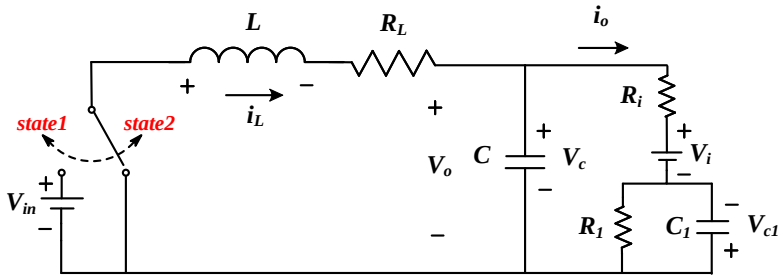


Figure 10. Equivalent circuit diagram of the buck converter and PEM electrolyzer.

The state variables of the system are selected as $x = [i_L(t), V_c(t), V_{c1}(t)]$, the input variables are $u = [V_{\text{in}}(t), V_i(t)]$, and the output variables are $y = [i_o(t), v_o(t)]$.

During one switching period, in state 1, the state-space averaged model of the buck converter over the time interval D_T is given by

$$\begin{cases} \dot{x} = A_1 x + B_1 u \\ y = C_1 x \end{cases} \tag{24}$$

It can be obtained from Kirchhoff's law that

$$\begin{cases} L\dfrac{di_L(t)}{dt} = V_{\text{in}}(t) - R_L i_L(t) - V_c(t) \\ C\dfrac{dV_c(t)}{dt} = i_L(t) + \dfrac{V_i(t) - V_c(t) - V_{c1}(t)}{R_i} \\ C_1\dfrac{dV_{c1}(t)}{dt} = \dfrac{-V_{c1}(t)}{R_1} + \dfrac{V_i(t) - V_c(t) - V_{c1}(t)}{R_i} \end{cases} \tag{25}$$

where i_L is the current on the inductor L. $V_{\text{in}}(t)$ and $V_i(t)$ are the input voltage and the reversible voltage of the PEM electrolyzer. $V_c(t)$ and $V_{c1}(t)$ are the voltage across the capacitor C and the equivalent capacitor C_1. R_L represents the equivalent parasitic resistance of the inductor. R_1 and R_i denote the equivalent resistances of the cathode and anode, respectively. Based on Equations (24) and (25), it can be deduced that

$$\begin{aligned} A_1 &= \begin{bmatrix} -\frac{R_L}{L} & -\frac{1}{L} & 0 \\ \frac{1}{C} & -\frac{1}{CR_i} & -\frac{1}{CR_i} \\ 0 & -\frac{1}{C_1 R_i} & -\frac{1}{C_1 R_1} - \frac{1}{C_1 R_i} \end{bmatrix} \\ B_1 &= \begin{bmatrix} \frac{1}{L} & 0 \\ 0 & \frac{1}{CR_i} \\ 0 & \frac{1}{C_1 R_i} \end{bmatrix} \quad C_1 = \begin{bmatrix} 1 \\ 1 \\ 0 \end{bmatrix} \end{aligned} \tag{26}$$

Combining state 2 during the time interval $1 - DT$, the state-space equations for the hydrogen production power source over the entire period T are given by

$$\begin{aligned} A &= DA_1 + (1-D)A_2 = \begin{bmatrix} -\frac{R_L}{L} & -\frac{1}{L} & 0 \\ \frac{1}{C} & -\frac{1}{CR_i} & -\frac{1}{CR_i} \\ 0 & -\frac{1}{C_1 R_i} & -\frac{1}{C_1 R_1} - \frac{1}{C_1 R_i} \end{bmatrix} \\ B &= DB_1 + (1-D)B_2 = \begin{bmatrix} \frac{D}{L} & 0 \\ 0 & \frac{1}{CR_i} \\ 0 & \frac{1}{C_1 R_i} \end{bmatrix} \\ C &= DC_1 + (1-D)C_2 = \begin{bmatrix} D \\ 1 \\ 0 \end{bmatrix} \end{aligned} \tag{27}$$

The input and control variables are represented as small-signal disturbances and substituted into the state-space expression. By separating the disturbance components, the small-signal state equation is derived as follows:

$$\begin{bmatrix} \frac{d\hat{i}_L(t)}{dt} \\ \frac{d\hat{v}_c(t)}{dt} \\ \frac{d\hat{v}_{c1}(t)}{dt} \end{bmatrix} = \begin{bmatrix} -\frac{R_L}{L} & -\frac{1}{L} & 0 \\ \frac{1}{C} & -\frac{1}{CR_i} & -\frac{1}{CR_i} \\ 0 & -\frac{1}{C_1R_i} & -\frac{1}{C_1R_1} - \frac{1}{C_1R_i} \end{bmatrix} \begin{bmatrix} \hat{i}_L(t) \\ \hat{v}_c(t) \\ \hat{v}_{c1}(t) \end{bmatrix} + \begin{bmatrix} \frac{D}{L} & 0 \\ 0 & \frac{1}{CR_i} \\ 0 & \frac{1}{C_1R_i} \end{bmatrix} \begin{bmatrix} \hat{v}_{\text{in}}(t) \\ \hat{v}_i(t) \end{bmatrix} + \begin{bmatrix} \frac{\hat{d}}{L} & 0 \\ 0 & \frac{1}{CR_i} \\ 0 & \frac{1}{C_1R_i} \end{bmatrix} \begin{bmatrix} V_{\text{in}}(t) \\ V_i(t) \end{bmatrix} \tag{28}$$

By applying the Laplace transform to the time-domain variables of the small-signal model, the system is converted into the complex frequency domain, allowing the derivation of the open-loop transfer function from duty cycle to output, from which the following can be deduced:

$$\begin{aligned} &\left.\frac{\hat{v}_o(s)}{d(s)}\right|_{v_i(s)=0} = V_{\text{in}} \frac{(C_1R_1R_i)s + (R_i + R_1)}{as^3 + bs^2 + cs + d} \\ &a = CC_1LR_iR_1 \\ &b = CLR_1 + C_1LR_1 + CLR_i + CC_1R_iR_1R_L \\ &c = L + C_1R_1R_i + CR_1R_L + C_1R_1R_L + CR_iR_L \\ &d = R_1 + R_i + R_L \end{aligned} \tag{29}$$

This third-order model reflects the fast LC filter dynamics of the Buck converter and the slower voltage response of the PEM electrolyzer.

To further examine the stability of the proposed DC-side bus voltage control strategy, the open-loop Bode diagram of the DC bus voltage control loop at a representative operating point is shown in Figure 11, where the parameters in (29) are taken from Section 5.1. The red vertical line indicates the gain crossover frequency (0 dB), and the black vertical line indicates the phase crossover frequency ($-180°$), used to determine phase and gain margins. The results indicate a phase margin of approximately 57°, while no gain crossover occurs at $-180°$ phase (corresponding to an infinite gain margin), demonstrating that the closed-loop system maintains a sufficiently large stability margin under the considered operating condition.

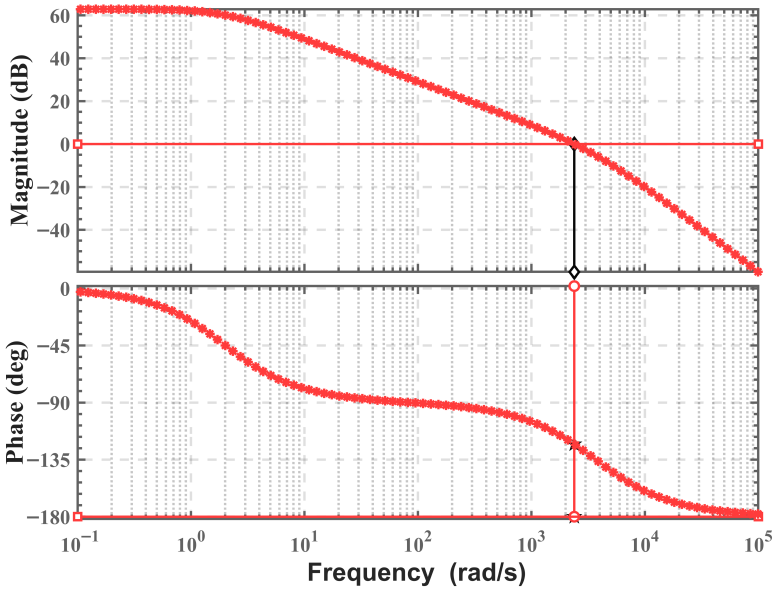


Figure 11. Bode plot of the open-loop transfer function of the output voltage.

4. Power Allocation Strategy

4.1. Simple Power Allocation Strategy

One commonly adopted power distribution method is the fixed equal-sharing strategy, in which a constant number of electrolyzer cells are operated and the input power is evenly distributed among them [27,28]. Although this approach ensures uniform power allocation, it performs poorly under low-power conditions. Due to the minimum operating threshold $P_{\min}$, the system cannot be activated when the available power is below $nP_{\min}$, leading to low renewable energy utilization. In addition, identical power profiles enforce synchronized start–stop behavior, resulting in frequent cycling at low power levels, which accelerates degradation and shortens the lifetime of the cells [29].

Another widely used method is the sequential (stepwise) power allocation strategy [30,31], where cells are activated one by one, with each preceding cell loaded to its rated power before the next is engaged. This approach expands the operating range and improves efficiency under low-power conditions. However, activating additional cells still requires the remaining power to exceed $P_{\min}$, leading to potential energy curtailment. Moreover, operating cells near rated or overload conditions reduces efficiency and accelerates aging, thereby degrading overall system performance and lifetime [32].

4.2. Degradation-Aware Power Allocation Strategy for PEMWE Arrays

According to the lifetime degradation analysis presented in Section B, the voltage degradation behavior of PEMWE stacks differs significantly between low-power and high-power operating regions. To explicitly distinguish these regimes, a turning power point P_t is introduced to partition the overall operating range.

For a PEMWE system with K individual stacks, the following hold:

- Low-Power Region ($P_{\text{wind}} < KP_t$): In this region, all activated stacks share the load according to a degradation-aware average allocation. Unlike a purely uniform distribution, the current assigned to each stack is weighted by its relative health, so that slightly degraded stacks carry proportionally less current. Specifically, a health indicator for each stack is defined as

$$H_i = \frac{1}{1 + \alpha \Delta V_i} \tag{30}$$

  where ΔV_i is the accumulated voltage degradation of the i-th stack and α is a sensitivity coefficient reflecting the impact of degradation on load participation. The proportional participation factor is computed as

$$w_i = \frac{H_i}{\sum_{j=1}^{N} H_j} \tag{31}$$

  and the preliminary current allocation becomes

$$I_i^* = w_i I_{\text{total}} \tag{32}$$

  This degradation-aware averaging ensures balanced operation even at low power levels and provides early mitigation of uneven aging.
- High-Power Region ($P_{\text{wind}} \geq KP_t$): When the total power demand exceeds the turning point, the system enters the high-power region, where degradation differences among stacks become more pronounced. To prevent the overloading of degraded stacks, a two-stage saturation–redistribution mechanism is applied. First, each stack current is constrained by an intermediate threshold I_M, and the residual current is calculated as

$$I_{\text{left}} = I_{\text{total}} - \sum_{i=1}^{N} \min(I_i^*, I_M) \tag{33}$$

Then, in the second stage, the remaining current I_{left} is progressively redistributed among the stacks according to their available margins until the rated current I_{elN} is reached:

$$I_i = \min(I_i + I_{\text{left}}, I_{\text{elN}}) \tag{34}$$

This two-stage approach ensures that healthier stacks naturally carry a larger share of the load under high-power conditions, while more degraded stacks are prevented from sustained high-current operation.

Overall, the proposed strategy forms a degradation-aware hierarchical allocation framework: it performs weighted average current sharing at low power to account for initial degradation differences, and implements a two-stage saturation-constrained redistribution at high power to ensure safe and balanced operation of all stacks.

5. Simulation Results

5.1. Parameter Setup and Test Scenario

To verify the feasibility of the proposed power marching strategy for the off-grid wind-to-hydrogen system, a simulation model was built on the MATLAB/Simulink (R2024a, The MathWorks, Inc., Natick, MA, USA) platform. In the experimental validation, a commercial PEM electrolyzer QLSC-H2 (Shandong Saikesaisi Hydrogen Energy Co., Ltd., Jinan, China) with a rated power of 3 kW was employed. The electrolyzer stack consists of multiple electrolysis cells connected in series and reflects a typical small-scale PEM electrolyzer stack configuration [33]. To bridge the gap between this experimental unit and the target MW-scale wind-to-hydrogen system, a structurally transferable control framework was adopted. Specifically, while the overall control structure remains unchanged, an engineering adaptation was carried out by re-identifying key system parameters and retuning control gains (e.g., low-pass filter constants and droop coefficients), so as to maintain dynamic stability and performance under MW-scale power and current levels. The main electrical and control parameters for the PMSG wind turbine system and the PEM electrolyzer system are listed in Tables 2 and 3.

The simulation cases are configured as follows: Section 5.2 presents the system operating performance under stepwise wind speed conditions. Section 5.3 presents the system performance under fluctuating natural wind speed conditions with noise. Section 5.4 provides a comparative analysis between the proposed control strategy and conventional control approaches. Section 5.5 investigates the electrolyzer power allocation performance under the proposed allocation strategy. Section 5.6 presents the parameter sensitivity analysis of the proposed method.

Table 2. Specific parameters of the PMSG wind turbine simulator.

Parameter	Value
Wind turbine diameter (D)	78 m
Air mass density (ρ)	1.225 kg/m^3
Stator phase resistance (R_s)	0.0259 Ω
Armature inductance (L_s)	1.5731 mH
Flux linkage (ψ_f)	9.0058 Wb
Number of pole pairs (n_p)	30
Cut-in wind speed ($V_w^{\min}$)	3 m/s
Cut-out wind speed ($V_w^{\max}$)	15 m/s
Threshold wind speed (V_w^{th})	12 m/s

Table 3. Specific parameters of the PEMWE and the converter.

Parameter	Value
Number of electrolyser cells (N)	220
Operating temperature (T)	353 K
Thickness of membrane (δ_m)	0.01275 mm
Active reaction area (A)	50 cm^2
Anode–electrolyte water activity (a_{H_2O})	1
Anodic exchange current density ($i_{o,a}$)	2×10^{-3} A/m^2
Cathodic exchange current density ($i_{o,c}$)	2×10^{-7} A/m^2
Anode charge transfer coefficient (α_a)	2
Cathodic charge transfer coefficient (α_c)	0.5
Maximum electrolyzer current (I^{max})	2200 A
DC-link inductor value (L)	30 mH
DC-link capacitor value (C)	666.67 µF

5.2. *Verification of System Operation Control Module*

The impact of the step change in wind speed on the operating point is shown in Figure 12. The wind speed starts at 11 m/s and increases in 1 m/s steps up to 14 m/s, and subsequently decreases back to 11 m/s,corresponding to operating points A, B, C, and D, respectively.

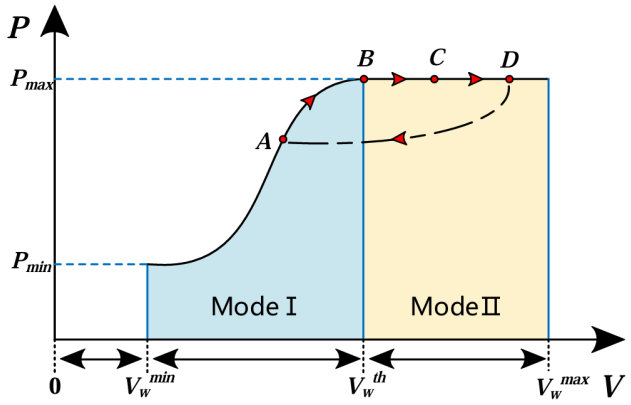


Figure 12. Experimental validation diagram illustrating the shifts in operating points.

Figure 13a illustrates the variations in the wind turbine pitch angle and rotor speed, where the subscript i in ω_i^{opt} indicates the optimal mechanical rotor speed at a wind speed of i m/s (i = 11, 12, 13, 14). Figure 13b shows the variations in the DC bus voltage and the electrolysis current of the PEMWE, while Figure 13c presents the power flow throughout the system. The I and II in the Figure 13 correspond to Mode I and Mode II respectively.

When the wind speed steps from 11 m/s to 12 m/s, it remains below the threshold V_w^{th} = 12 m/s. At this stage, the system operates in the MPPT region, the pitch angle remains inactive, and the rotor speed adjusts to maintain maximum power tracking. As the wind speed increases from 12 m/s to 13 m/s, it exceeds the rated value. The rotor speed reaches 21.92 rpm, which is still below the optimal speed of 25.78 rpm at 13 m/s. The pitch control begins to engage to prevent excessive power transmission that could damage the electrolyzer. This indicates that the PEMWE is gradually reaching its power absorption limit, prompting the wind turbine to restrict its power output. The electrolysis current on the PEMWE side increases and stabilizes at I^{max} = 2200 A, marking the maximum operational state of the electrolyzer. As the wind speed steps up further to 14 m/s, the rotor speed becomes increasingly constrained, and the pitch angle continues to rise. After a brief overshoot, the electrolysis current remains steady at 2200 A. The wind turbine output,

the electrolyzer's power consumption, and the hydrogen production rate all show negligible change, indicating that the system is operating in a power-limiting mode. Finally, when the wind speed rapidly drops and passes below the rated value, the rotor speed decreases accordingly and eventually tracks the optimal speed corresponding to 11 m/s, while the pitch angle simultaneously returns to its original position. Throughout the step wind speed variations, the DC bus voltage remains stable, ensuring real-time power balance in the off-grid system.

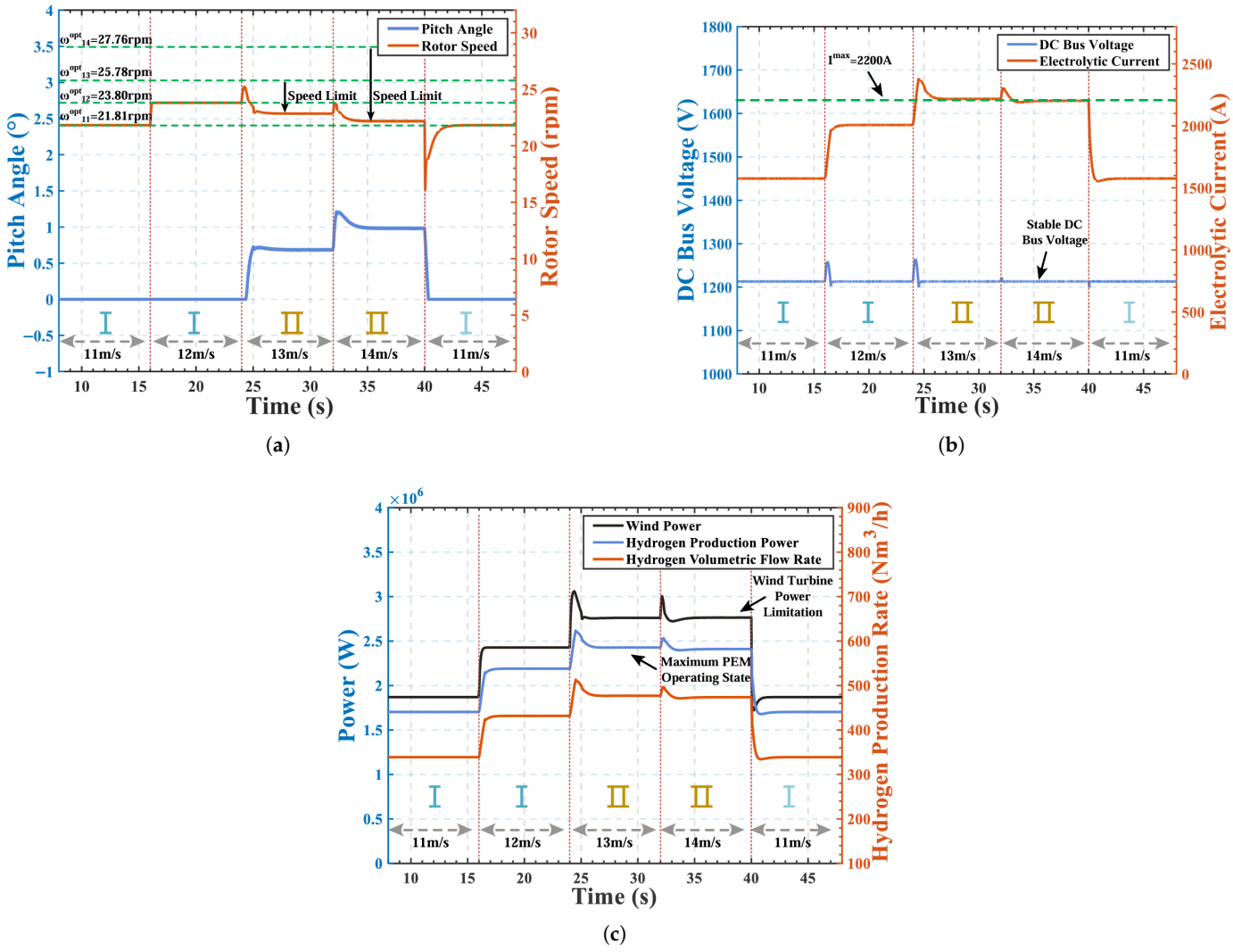


Figure 13. System performance under stepwise wind conditions: (**a**) Pitch angle and rotor speed; (**b**) DC voltage and current; (**c**) Power and hydrogen production.

5.3. Simulation Under Natural Wind Conditions

Wind energy in nature is characterized by randomness, intermittency, and other features. In this section, a combination of four component models—basic wind, gusts, gradual winds, and random winds—was used for simulation testing of the off-grid system. The wind speed begins to vary in a sinusoid-like waveform starting from 12 m/s, as Figure 14a depicts.

It can be clearly observed that once the wind speed exceeds the threshold V_w^{th}, parameters such as system power and hydrogen production rate reach their maximum values and remain saturated without further increase. As shown in Figure 14d, the electrolysis power of PEM accurately tracks the power output of the wind turbine throughout the operation, with both power and hydrogen production exhibiting a stable variation trend.

During the entire operating condition, the DC bus voltage remains at a stable level, and the system smoothly transitions between the MPPT mode and the constant power mode during dynamic changes, maintaining stability throughout the off-grid operation.

This shows that the control strategy limits output beyond the threshold to avoid overloading, while the coordinated response of the wind turbine and PEM electrolyzer ensures robust, reliable, and efficient operation under fluctuating wind conditions.

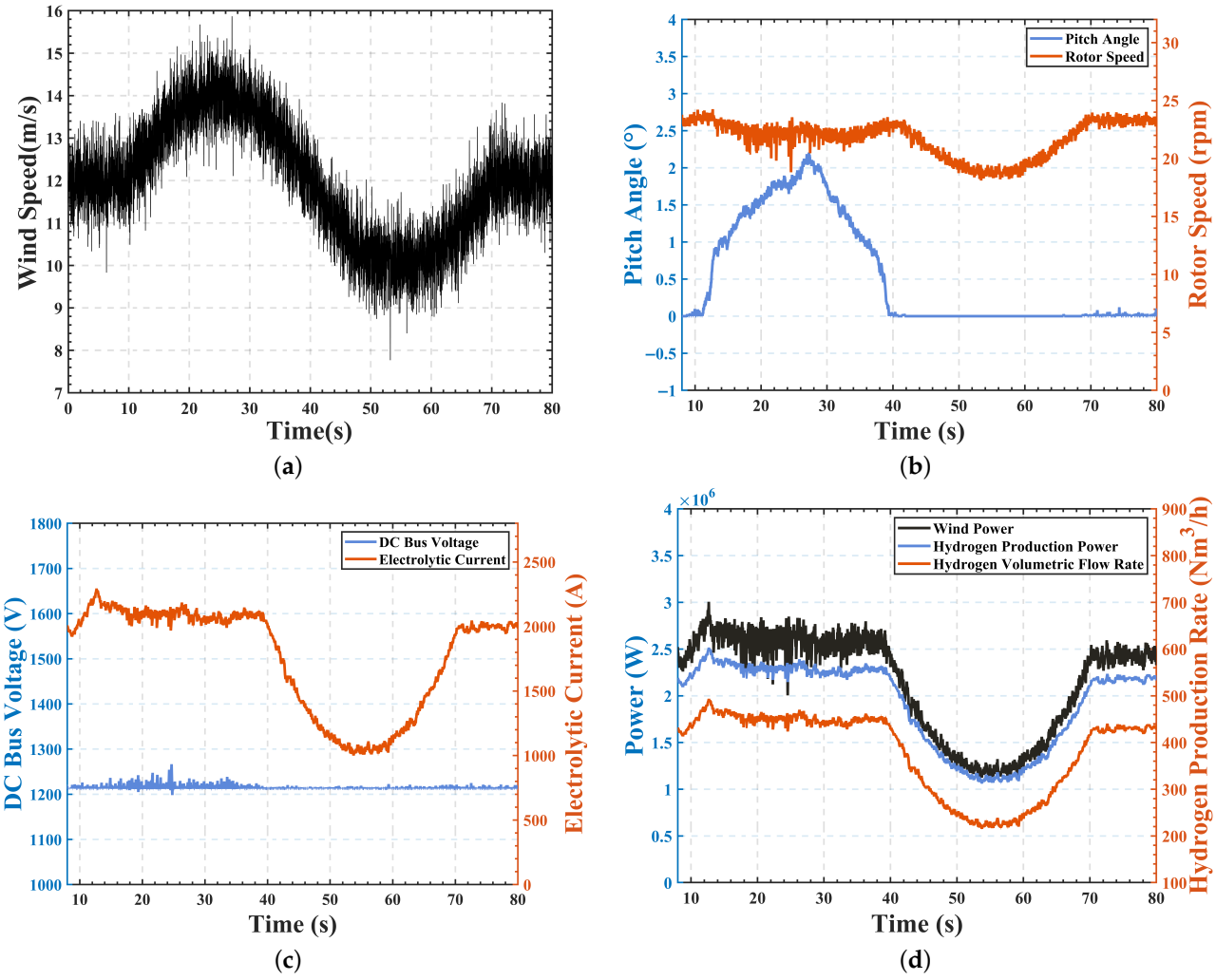


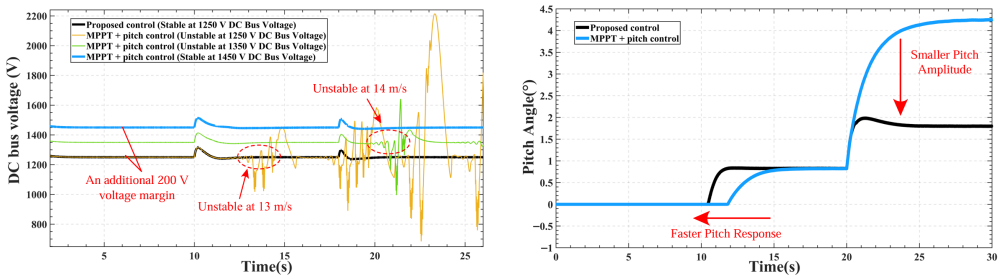
Figure 14. Simulation experiment under natural fluctuating wind speed. (**a**) Natural wind with added noise. (**b**) Variation in blade pitch angle and rotor speed. (**c**) Variation in DC bus voltage and electrolytic current. (**d**) Variation in wind power, hydrogen production power and hydrogen volumetric flow rate.

5.4. Improved Dynamic Response Through the Proposed Coordination Control

Maximum power point tracking combined with pitch angle regulation is a widely adopted output control strategy in variable-speed wind turbine systems. However, in off-grid systems, the lack of grid support and the nonlinear characteristics of the electrolyzer increase the system sensitivity to wind disturbances. The control strategy proposed in this paper limits the wind energy ramp rate during sudden wind variations, thereby suppressing DC bus voltage fluctuations and reducing the required pitch adjustment for faster stabilization.

Figure 15 presents a representative wind speed step disturbance scenario used to compare the dynamic response characteristics of the two control strategies. As shown in the

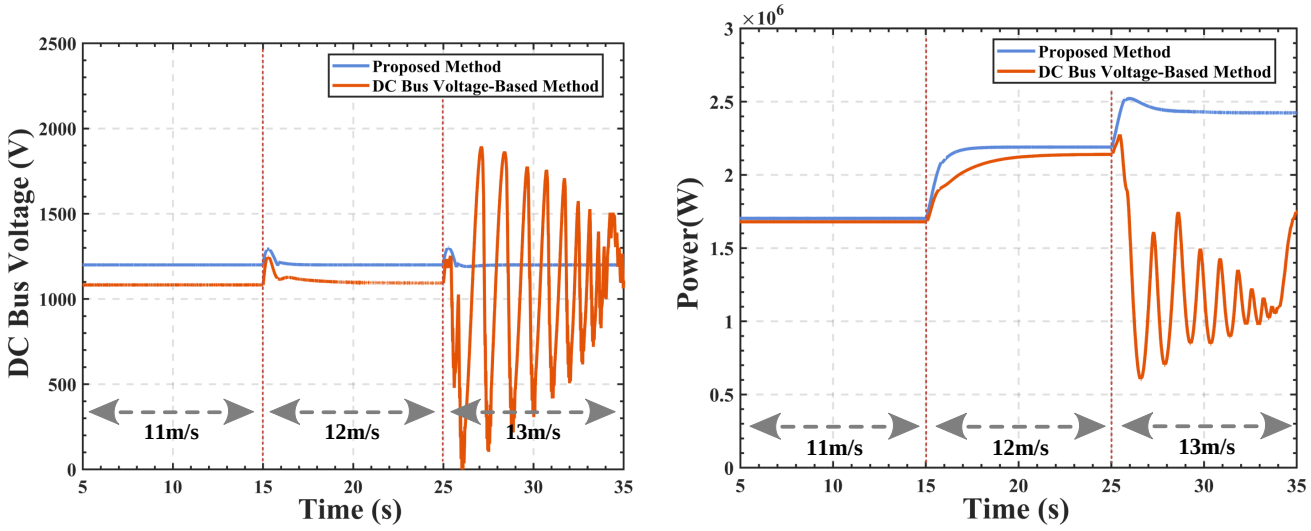
figure, the proposed control strategy results in a lower stabilized DC voltage and smaller pitch angle variation, indicating improved steady-state and transient performance.



(**a**) (**b**)

Figure 15. Enhanced dynamic performance under step wind input with the proposed control scheme. (**a**) Improved voltage stability at lower setpoints enabled by proposed control. (**b**) Reduced pitch angle deviation and faster stabilization enabled by proposed control.

Some researchers have proposed a power control method for FOWT based on DC bus voltage information, in which the voltage–speed relationship is regulated according to the DC bus voltage level [33]. Figure 16 presents simulations under the same conditions as the previous experiments to compare the system performance of the two control strategies under varying wind speeds.



(**a**) (**b**)

Figure 16. Comparison of system responses to step wind speed changes under different control strategies. (**a**) Bus voltage variation. (**b**) System power variation.

Under wind speed variations between 11 m/s and 12 m/s, the droop control based on bus voltage becomes active, resulting in a slight increase in the bus voltage. Although the overall system remains stable at this point, its power response time is longer than that of the proposed method. As the wind speed continues to increase, power fluctuations in the wind turbine system become more pronounced under high wind conditions. The rotor speed undergoes larger adjustments, and in the absence of pitch angle regulation to limit the input power, it becomes difficult to maintain the power balance between the source and load in the off-grid system. Consequently, the DC bus voltage drops significantly, leading to system instability.

Beyond the high wind speed conditions discussed above, the performance of the proposed control strategy is further evaluated under normal operating wind speeds ranging

from 11 m/s to 12 m/s, as shown in Figure 17. In this operating region, the system operates below the rated limits, and no protective or power-limiting actions are activated. To assess the robustness of the control strategy under realistic conditions, the system is subjected to naturally fluctuating wind profiles within this range. These fluctuations introduce small but non-negligible variations in input power, allowing for a detailed examination of the control strategy's ability to maintain voltage stability, rotor speed regulation, and power balance. The results provide insight into how effectively the proposed method can mitigate the impact of short-term wind disturbances and maintain reliable operation even under variable wind conditions.

Under fluctuating wind speed with stochastic noise, the proposed control strategy significantly suppresses DC-link voltage fluctuations, reducing the voltage RMS deviation by 74.5%, demonstrating the enhanced robustness and energy conversion effectiveness of the proposed method under noisy wind conditions. The detailed quantitative results are summarized in Table 4.

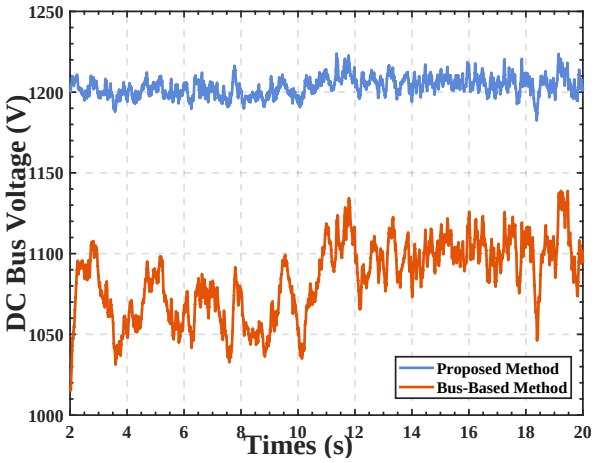


Figure 17. Bus voltage variation under noisy natural wind speed fluctuations with different control strategies.

Table 4. Performance comparison under noisy wind conditions.

Metric	Conventional	Proposed
Mean DC voltage (V)	1084.5	1203.4
Voltage RMS deviation (V)	23.25	5.94
Voltage variance (V^2)	540.7	35.3

5.5. Verification of Power Allocation Control Module

To verify the effectiveness of the proposed control strategy, open-access measured wind power data from the Walloon Region of Belgium are employed. Specifically, a typical low-wind month in summer (June 2025) and a typical high-wind month in winter (December 2025) are selected to capture seasonal variations and enhance the representativeness of the analysis. The data are obtained from the Elia wind power generation data portal (https://www.elia.be/en/grid-data/generation-data/wind-power-generation) (accessed on 17 January 2026). The original dataset is resampled with a 3-h time step, corresponding to one discrete simulation interval. The processed wind power output profiles are illustrated in Figure 18.

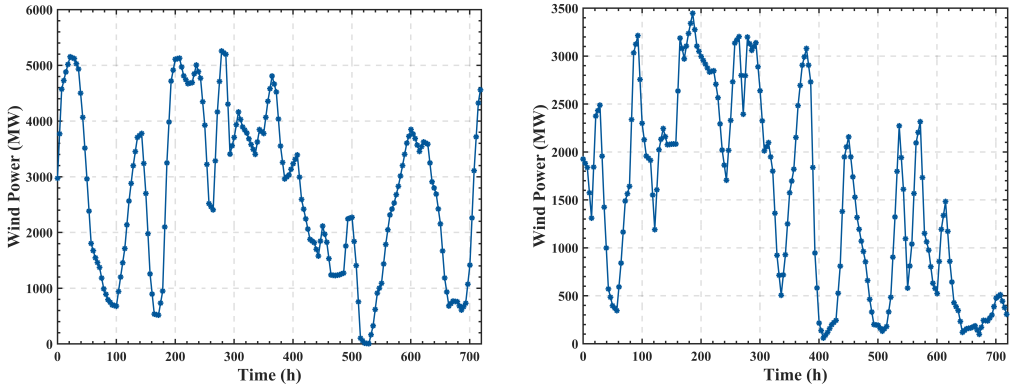


Figure 18. Measured wind power data. (**a**) Typical high-wind month in winter. (**b**) Typical low-wind month in summer.

Three power allocation strategies are considered for comparative analysis: Strategy 1 adopts a sequential (stepwise) power allocation approach; Strategy 2 employs a fixed equal-sharing strategy; and Strategy 3 applies the proposed two-stage, bi-layer power allocation strategy with degradation awareness.

Figure 19 illustrates the power allocation results of individual electrolyzer stacks under different power distribution strategies. It can be observed that Strategy 1 adopts a sequential power allocation scheme, in which the system prioritizes power delivery to the upstream electrolyzers and activates subsequent stacks only after the preceding ones reach their rated power. As a result, Electrolyzer 1 remains continuously in operation and operates at high load or even overload levels during most periods. Owing to the strong fluctuations of wind and solar power, Electrolyzers 2–4 experience frequent start–stop operations and, when activated, often operate in the overload region, while Electrolyzer 5 is only engaged during a few high-power periods and remains idle most of the time.

Strategy 2 employs a fixed equal power distribution strategy, in which all electrolyzers are always activated simultaneously and receive identical power allocations. During periods of low wind and solar power, all electrolyzers operate under low-load conditions or are shut down simultaneously. This results in overlapping lines in the figure due to the uniform power allocation, and the same applies to the following figures.

Strategy 3 adopts the proposed degradation-aware bi-layer power allocation strategy. While satisfying the system power demand, the health state information of individual electrolyzers is incorporated into the coordinated control framework. Under high-load or short-term overload conditions, electrolyzers with higher health levels are preferentially assigned more power; under low-load conditions, power is likewise allocated according to the degradation states of individual electrolyzers. In addition, the integration of auxiliary power support enables the system to avoid large-scale shutdowns.

Under low-wind conditions in summer, as shown in Figure 20, the available renewable power is frequently insufficient to sustain full-load operation of all electrolyzer stacks. In Strategy 2 (fixed equal-sharing), the limited input power is uniformly distributed among all stacks, causing each electrolyzer to operate at very low load levels or even fall below the minimum operating threshold, which leads to simultaneous shutdowns. This results in frequent start–stop cycles that accelerate degradation and shorten the operational lifetime of the electrolyzers.

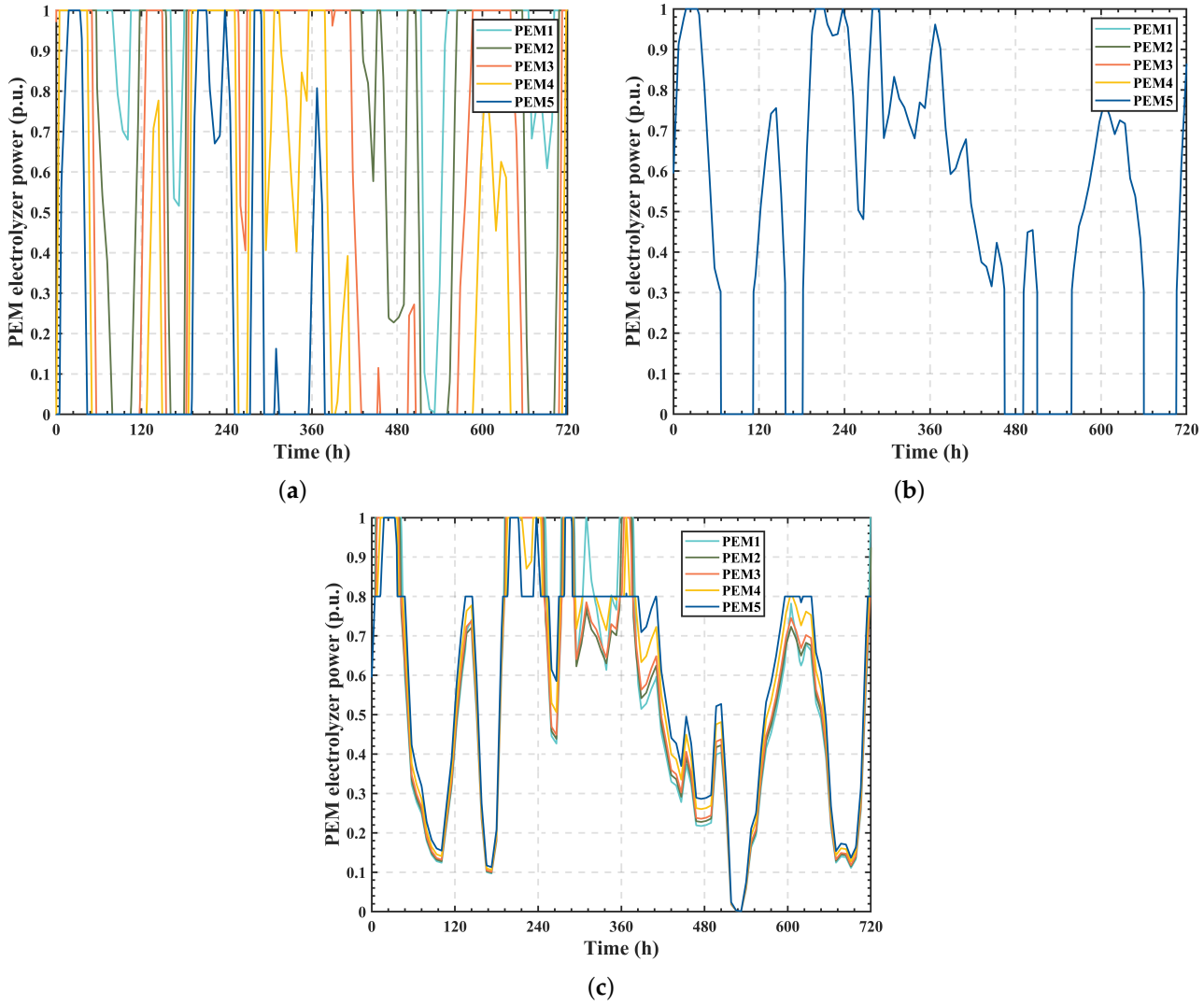


Figure 19. Power allocation of each PEMWE single stack under high-wind conditions in winter under (**a**) Strategy 1, (**b**) Strategy 2, and (**c**) Strategy 3.

In contrast, Strategy 3, which incorporates the proposed degradation-aware bi-layer power allocation with auxiliary power support, demonstrates improved operational robustness under low-wind conditions. By dynamically allocating power based on both system demand and the degradation states of individual stacks, the strategy prioritizes maintaining the stable operation of selected electrolyzers rather than uniformly distributing insufficient power.

The voltage degradation of individual PEMWE stacks under different power allocation strategies is illustrated in Figure 21. It can be observed that the impacts of different strategies on the voltage degradation characteristics of single stacks differ significantly.

Under Strategy 1, voltage degradation is highly non-uniform. Upstream PEMWE 1 experiences sustained high-load conditions, with cumulative degradation reaching 9.6 mV, while other stacks undergo minimal degradation (as low as 1.2 mV). This sequential allocation leads to concentrated power distribution and uneven operating stress, accelerating aging of some stacks and limiting the overall system lifetime.

Under Strategy 2, all stacks operate synchronously, and their voltage degradation levels remain relatively close to each other, with an overall degradation magnitude of approximately 2.9 mV.

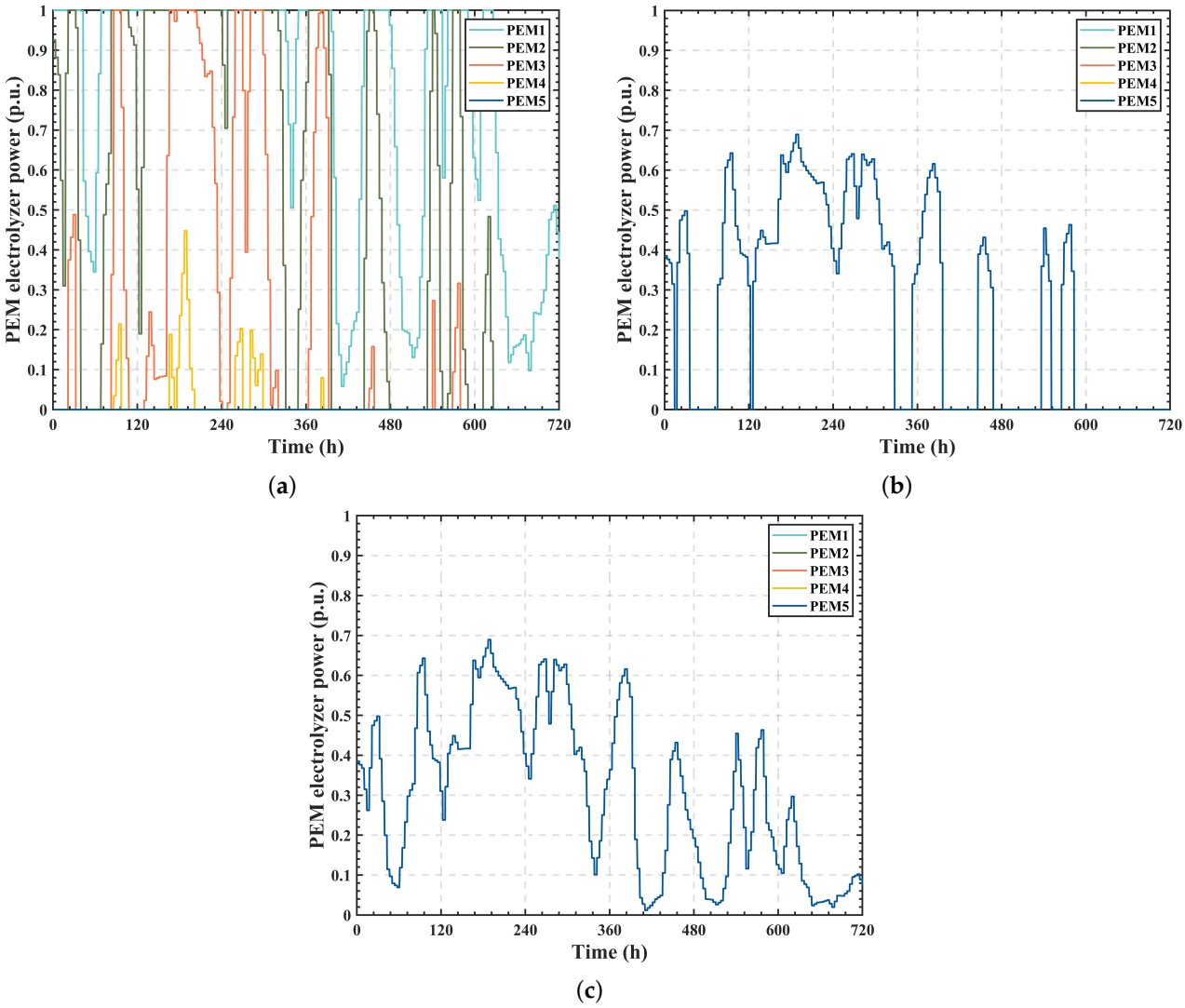


Figure 20. Power allocation of each PEMWE single stack under low-wind conditions in summer under (**a**) Strategy 1, (**b**) Strategy 2, and (**c**) Strategy 3.

Strategy 3 effectively balances the operating stress among PEMWE stacks. By considering the health state during power allocation, stack voltage degradation is maintained within a narrow range of 3.6–4.4 mV, improving degradation uniformity and extending the system's overall service lifetime.

From the previous operating conditions of the electrolyzers under low-wind scenarios, it can be seen that the low voltage degradation observed in Strategy 2 is largely due to the collective shutdown of the electrolyzers. Compared with the advantages of Strategy 3, this benefit is not significant and, in fact, introduces the risk of frequent start–stop cycles.

The comparison of hydrogen production efficiency across different power allocation strategies can be summarized from both horizontal (strategy-to-strategy) and vertical (seasonal condition) perspectives in Figure 22.

Horizontal comparison (strategy performance): Strategy 1 (a, b)—fluctuating control: The efficiency curve exhibits high-frequency, small-amplitude oscillations. Although the overall efficiency generally remains around 0.4–0.5, during the low-wind summer months (Figure 22b) the fluctuations become pronounced, with a clear downward trend at times. This indicates that Strategy 1 is highly sensitive to variations in input power and demonstrates relatively poor operational stability.

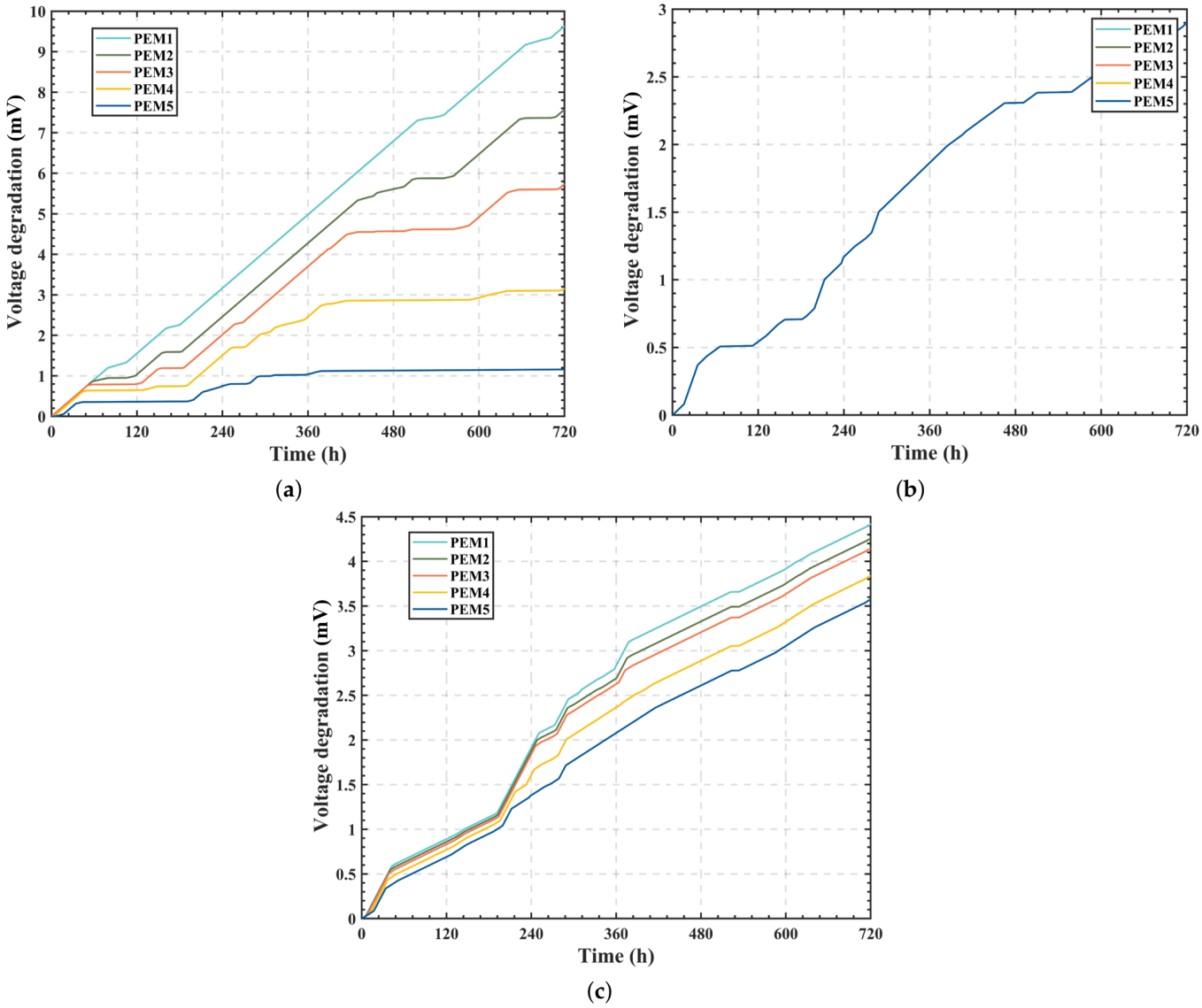


Figure 21. Different voltage degradation of each PEMWE stack under (**a**) Strategy 1, (**b**) Strategy 2, and (**c**) Strategy 3.

Strategy 2 (c, d)—Intermittent/start–stop control: Large regions of zero efficiency appear, reflecting frequent start–stop behavior. Under insufficient power, some electrolyzers are shut down, while during operation, the instantaneous efficiency can reach peaks of 0.6 or higher. Although this approach avoids inefficient low-load operation, the frequent cycling imposes a high risk of accelerated equipment degradation and results in poor continuity.

Strategy 3 (e, f)—smooth/robust control: The efficiency curve is the smoothest among the three strategies, with clearly smaller fluctuations than Strategy 1. This strategy consistently achieves the best performance, maintaining high average efficiency (0.45–0.6) in the winter high-wind months and preserving operational stability during the summer low-wind months. Occasional short-term drops recover rapidly, demonstrating superior robustness.

Vertical comparison (seasonal impact): Winter high-wind month (a, c, e): Sufficient and relatively stable wind power allows electrolyzers to operate at higher and more continuous input levels. All three strategies achieve higher efficiency and more continuous operation, with baseline efficiency typically above 0.4.

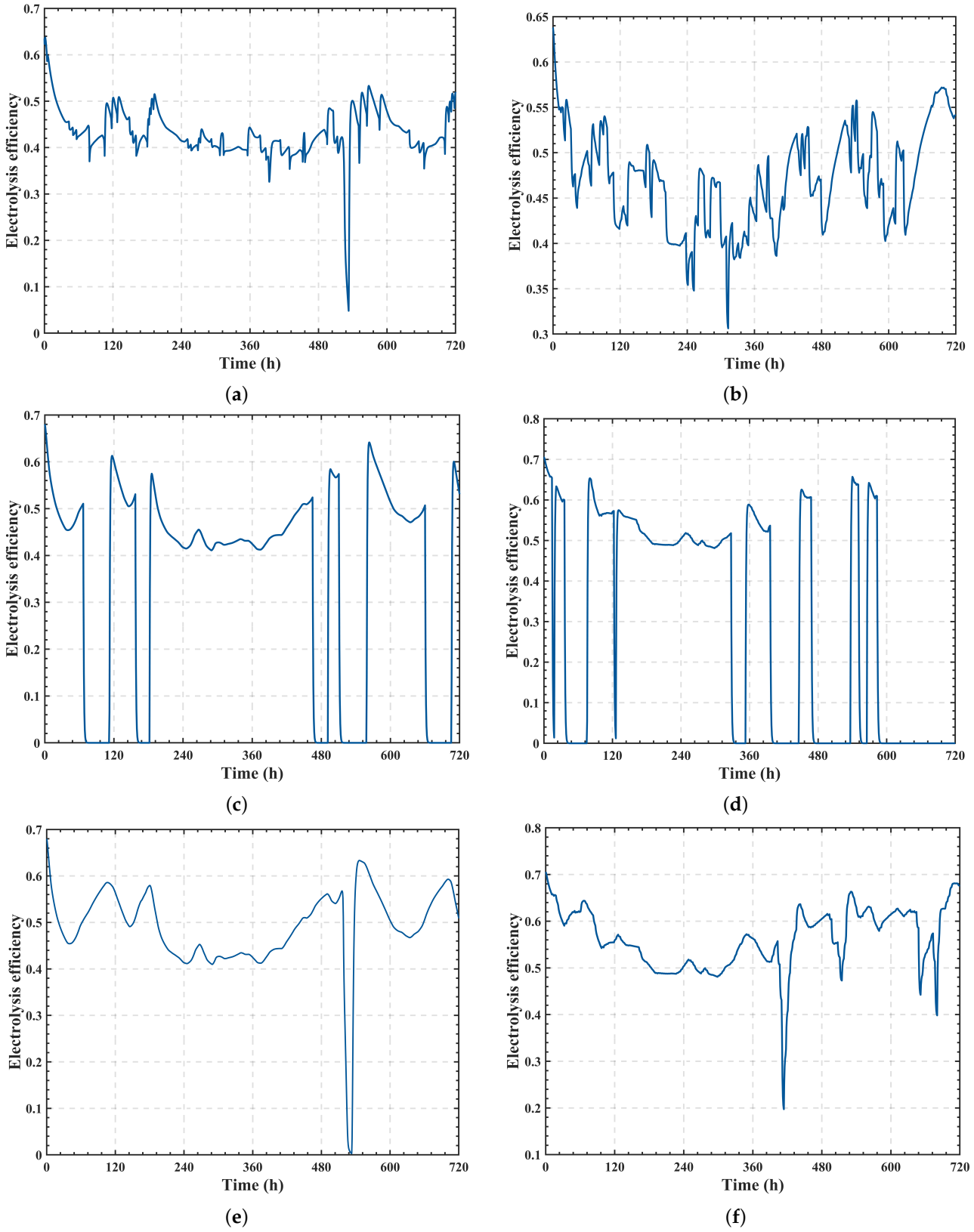


Figure 22. Electrolysis efficiency of each PEMWE single-stack under different power allocation strategies. Each row corresponds to a strategy: (**a**,**b**) Strategy 1, (**c**,**d**) Strategy 2, (**e**,**f**) Strategy 3.

Summer low-wind months (b, d, f): Lower and more fluctuating wind power causes the system to frequently operate under partial or very low loads. As a result, efficiency drops significantly or exhibits strong fluctuations for all strategies. In Figure 22d, this is

reflected in frequent shutdown events, while in Figure 22b, efficiency shows irregular oscillations. These observations indicate that low-wind conditions impose greater challenges for the power allocation and coordination capabilities of the control algorithms.

5.6. Robustness and Sensitivity Analyses Under Parameter Uncertainties

To evaluate the performance of the proposed off-grid wind–hydrogen system under representative modeling uncertainties and non-ideal operating conditions, both robustness and sensitivity analyses were conducted. The robustness simulations primarily consider variations in key generator electrical parameters, including stator resistance, stator inductance, and permanent magnet flux linkage, together with DC bus voltage measurement delays. In addition, a sensitivity analysis was carried out with respect to key mechanical-side parameters, namely inertia and viscous damping, to investigate how realistic variations in wind turbine dynamics affect the controller performance and DC-side voltage regulation. This section considers wind speed conditions with superimposed noise, as described in Section 5.3.

The robustness simulation results corresponding to Figure 23 indicate that, overall, the proposed system is able to maintain stable DC bus voltage regulation under representative 10% variations of key generator parameters as well as different measurement delays, suggesting a reasonable level of robustness from a system-level perspective. As shown in Figure 23a, the DC bus voltage responses under generator parameter variations remain closely clustered, and both transient and steady-state deviations are relatively small, indicating a limited sensitivity to the considered parameter uncertainties. In contrast, Figure 23b shows that measurement delays exert a more noticeable influence on the DC bus voltage dynamics, particularly during transient periods, although the overall system stability is still preserved.

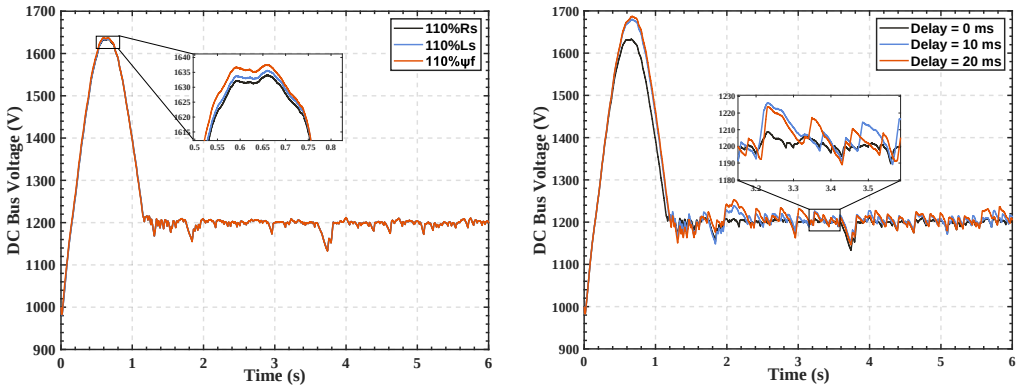
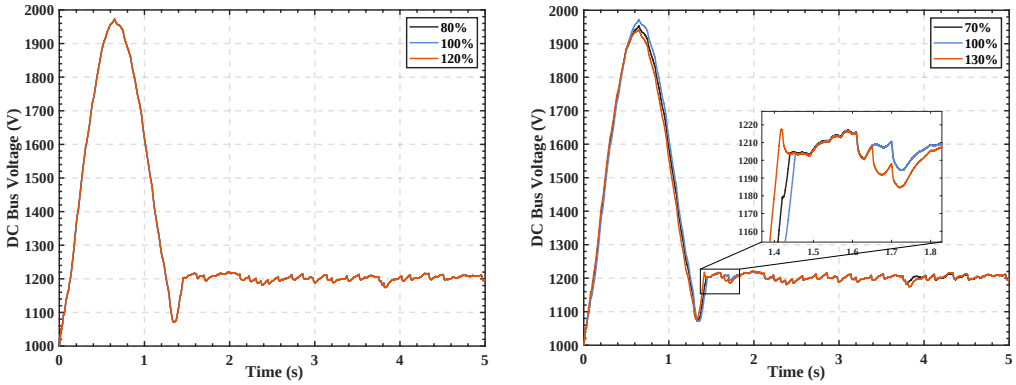


Figure 23. Robustness evaluation of the system under parameter uncertainties and measurement delays. (**a**) DC bus voltage responses with 10% generator parameter variations. (**b**) DC bus voltage responses under different DC bus voltage measurement delays.

The sensitivity analysis is shown in Figure 24 and indicates that variations in inertia within the considered ranges have a negligible impact on the DC bus voltage dynamics, while changes in viscous damping introduce moderate differences in the transient response. This behavior can be attributed to the time-scale separation between the mechanical and electrical subsystems, as well as the regulating effect of the proposed DC-side control strategy, which effectively attenuates slow mechanical disturbances and power fluctuations. In contrast, viscous damping directly affects the decay of speed and torque oscillations, leading to observable but bounded variations in voltage transients. Overall, the results

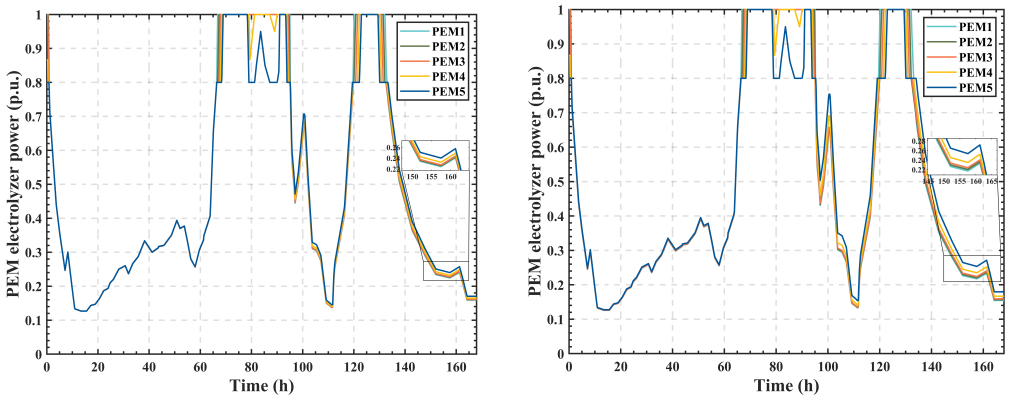
demonstrate that the proposed control strategy maintains stable and robust DC voltage regulation under realistic mechanical parameter uncertainties.



(**a**) (**b**)

Figure 24. Sensitivity analysis of controller performance under mechanical parameter variations. (**a**) DC bus voltage responses with ±20% inertia variations. (**b**) DC bus voltage responses with ±30% viscous damping variations.

To investigate the impact of the degradation sensitivity coefficient α on load allocation, Figure 25 compares the current distribution among PEMWE stacks for $\alpha = 1$ and $\alpha = 5$. A larger α increases the sensitivity of the stack health indicator H_i to accumulated voltage degradation ΔV_i, resulting in a greater difference in allocated power between healthy and degraded stacks. Conversely, a smaller α yields a more uniform current distribution, approaching equal-load operation. It should be noted that the value of α must be matched to the magnitude of ΔV_i, and excessively large α may lead to transient overloading of healthier stacks under fast power fluctuations.



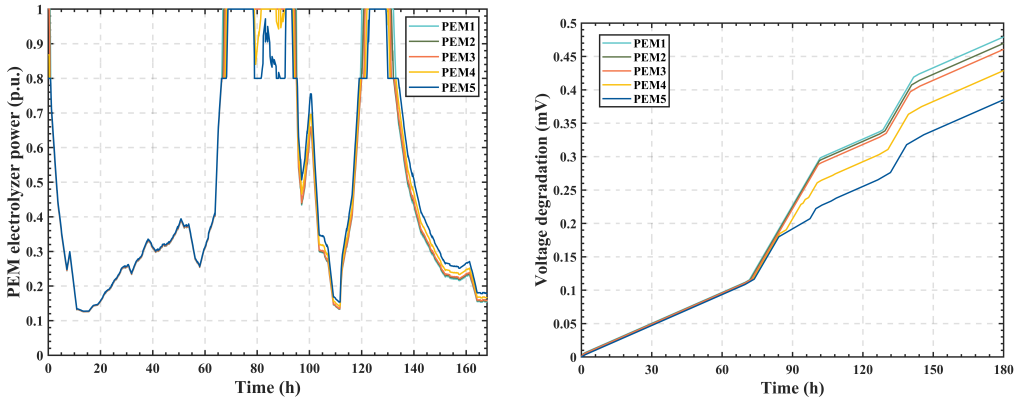
(**a**) (**b**)

Figure 25. Sensitivity analysis of load allocation with respect to the degradation sensitivity coefficient α. (**a**) Current distribution among PEMWE stacks for $\alpha = 1$. (**b**) Current distribution among PEMWE stacks for $\alpha = 5$.

To quantitatively evaluate the robustness of the proposed health-indicator-based power allocation strategy under measurement uncertainty, based on the previously defined sensitivity coefficient $\alpha = 5$, a $\pm$ 5% uniformly distributed random noise is introduced into the current measurement used for degradation estimation, as shown in Figure 26. The noisy measurement is modeled as

$$I_{\text{meas}} = I(1 + \delta), \quad \delta \in [-0.05, 0.05], \tag{35}$$

which is implemented in Simulink using a Uniform Random Number block with fixed bounds and a constant seed to ensure reproducibility. The resulting power allocation under noisy conditions shows that, in the second high-power operating region, electrolyzers that do not reach their rated power exhibit slight fluctuations due to noise perturbations, whereas in all other operating regions the allocation remains essentially unchanged. Compared with the noise-free case shown in Figure 25b, the overall power distribution pattern remains highly consistent, and the corresponding voltage degradation curves maintain a smooth trend, indicating that the cumulative degradation-based health indicator effectively suppresses short-term disturbances and ensures robust system performance.



(**a**) (**b**)

Figure 26. Impact of measurement noise on power allocation and degradation behavior. (**a**) Power distribution among PEMWE stacks with ±5% measurement noise. (**b**) Voltage degradation trajectories of PEMWE stacks with ±5% measurement noise.

6. Conclusions

This paper focuses on the power allocation and stable operation of electrolyzer arrays in off-grid wind–solar hydrogen production systems. To address the operational challenges arising from the strong stochasticity of wind power and its coupling with electrolyzer degradation, system modeling, control strategy design, and simulation-based validation are conducted. The main conclusions are summarized as follows:

(1) Based on the electrochemical mechanisms of PEMWEs, a single-cell electrochemical model is established. On this basis, a lifetime model characterized by the voltage degradation rate is introduced to quantify the degradation degree of the electrolyzer. The intrinsic relationships among operating power, operating conditions, and voltage degradation are clarified, providing a theoretical foundation for subsequent power allocation and lifetime-coordinated control.

(2) A wind turbine power control method combining wind speed–rotor speed droop characteristics and pitch angle regulation is proposed to compensate for the energy mismatch between the wind turbine and the electrolyzer. Compared with conventional methods, the proposed approach enhances the system's response to uncertainties such as high wind-speed fluctuations and improves dynamic performance: the RMS deviation of the DC bus voltage is reduced by 17.31%, and both the pitch angle response time and adjustment amplitude are significantly decreased. Compared with other bus-voltage-based control methods, this approach exhibits better stability under larger disturbances.

(3) On the electrolyzer side, a degradation-aware power allocation strategy for off-grid wind–solar hydrogen production systems is proposed. Simulation results show that, compared with conventional fixed equal power allocation and sequential allocation strategies, the proposed degradation-aware method can effectively slow down uneven system lifetime degradation, significantly reduce start–stop operations, improve renewable

energy utilization, and maintain high hydrogen production efficiency and stable output across the full operating power range.

Author Contributions: F.Y. and X.L.: writing—original draft preparation; D.L.: writing—review and editing; Y.D.: review and editing; X.L.: methodology; D.L.: validation; Y.D.: supervision. All authors have read and agreed to the published version of the manuscript.

Funding: This research was funded by the National Natural Science Foundation of China (Grant No. 52377111).

Data Availability Statement: The original contributions presented in this study are included in the article. Further inquiries can be directed to the corresponding author.

Conflicts of Interest: The authors declare no conflicts of interest.

References

1. Ren, G.; Liu, J.; Wan, J.; Guo, Y.; Yu, D. Overview of wind power intermittency: Impacts, measurements, and mitigation solutions. *Appl. Energy* **2017**, *204*, 47–65. [CrossRef]
2. Tan, R.; Jing, Z.; Wang, Y.; Zhao, Z. An effective scheduling strategy for offshore wind farm maintenance optimization considering multi-practical operation conditions. *Protect. Control Mod. Power Syst.* **2025**, *10*, 133–149. [CrossRef]
3. Liang, Y.; Lin, S.; Lai, X.; Liu, M.; Zhang, B. Coordinated planning for multiple inner networks of offshore wind farms and onshore transmission expansion. *Protect. Control Mod. Power Syst.* **2025**, *10*, 35–54. [CrossRef]
4. Kudria, S.; Ivanchenko, I.; Tuchynskyi, B.; Petrenko, K.; Karmazin, O.; Riepkin, O. Resource potential for wind–hydrogen power in Ukraine. *Int. J. Hydrogen Energy* **2021**, *46*, 157–168. [CrossRef]
5. Wang, X.; Li, B.; Wang, Y.; Lu, H.; Zhao, H.; Xue, W. A bargaining game-based profit allocation method for the wind–hydrogen–storage combined system. *Appl. Energy* **2022**, *310*, 118472. [CrossRef]
6. Du, Y.; Shen, X.; Kammen, D.M.; Ding, X. Cost-competitive offshore wind-powered green methanol production for maritime transport decarbonization. *Nat. Commun.* **2025**, *16*, 5453. [CrossRef]
7. Misra, H.; Gundavarapu, A.; Jain, A.K. Control scheme for DC voltage regulation of stand-alone DFIG–DC system. *IEEE Trans. Ind. Electron.* **2017**, *64*, 2700–2708. [CrossRef]
8. Zhang, J.; Xiao, F.; Ma, F.; Xiao, R. Dynamic characteristics simulation of medium voltage DC off-grid hydrogen production system. In Proceedings of the IEEE/IAS Industrial and Commercial Power Systems Asia, Chongqing, China, 7–9 July 2023.
9. Zhu, X.; Chen, J.; Wang, P.; Wu, Z.; Zhu, L.; Fang, Z. A novel wind turbine control method for mitigating power fluctuations and cooperative capacity configuration for the stand-alone wind hydrogen generation system. In Proceedings of the IEEE 19th Conference on Industrial Electronics and Applications, Kristiansand, Norway, 5–8 August 2024.
10. Mao, X.; Tian, Y.; Yang, A.; Zhang, G. Identification of equivalent circuit parameters for proton exchange membrane (PEM) electrolyzer engineering models. *IEEE Access* **2024**, *12*, 15509–15524. [CrossRef]
11. Guilbert, D.; Vitale, G. Dynamic emulation of a PEM electrolyzer by time constant based exponential model. *Energies* **2019**, *12*, 750. [CrossRef]
12. Wang, Z.; Tang, Y.; Shi, C.; Guo, L. Power balance control of an energy-storage-free islanded offshore wind hydrogen production system. *Electr. Power Syst. Res.* **2025**, *245*, 111558. [CrossRef]
13. Zhang, X.; Liu, Y.; Zhang, Y.; Tan, W.; Hao, S.; Huang, C. An improved voltage–power control strategy of wind power-to-hydrogen systems considering hydrogen high sensitivity factors. *Electr. Power Syst. Res.* **2025**, *247*, 111763. [CrossRef]
14. Weiss, A.; Siebel, A.; Bernt, M.; Shen, T.H.; Tileli, V.; Gasteiger, H.A. Impact of intermittent operation on lifetime and performance of a PEM water electrolyzer. *J. Electrochem. Soc.* **2019**, *166*, F487–F497. [CrossRef]
15. Frensch, S.H.; Fouda-Onana, F.; Serre, G.; Thoby, D.; Araya, S.S.; Kær, S.K. Influence of the operation mode on PEM water electrolysis degradation. *Int. J. Hydrogen Energy* **2019**, *44*, 29889–29898. [CrossRef]
16. Maniscalco, M.P.; Culcasi, A.; Asaro, S.; Ferraro, M. Hydrogen from seawater: An environmental and economic evaluation of AEM and PEM electrolysis coupled with advanced desalination systems. *Chem. Eng. Trans.* **2025**, *119*, 97–102.
17. Fang, R.; Liang, Y. Control strategy of electrolyzer in a wind–hydrogen system considering the constraints of switching times. *Int. J. Hydrogen Energy* **2019**, *44*, 25104–25111. [CrossRef]
18. Jing, K.; Liu, C.; Cao, X.; Sun, H.; Dong, Y. Analysis, modeling and control of a non-grid-connected source–load collaboration wind–hydrogen system. *J. Electr. Eng. Technol.* **2021**, *16*, 2355–2365. [CrossRef]
19. Muyeen, S.M.; Takahashi, R.; Tamura, J. Electrolyzer switching strategy for hydrogen generation from variable speed wind generator. *Electr. Power Syst. Res.* **2011**, *81*, 1171–1179. [CrossRef]

20. Wang, X.; Meng, X.; Nie, G.; Li, B.; Yang, H.; He, M. Optimization of hydrogen production in multi-electrolyzer systems: A novel control strategy for enhanced renewable energy utilization and electrolyzer lifespan. *Appl. Energy* **2024**, *376*, 124299. [CrossRef]
21. Hong, Z.; Wei, Z.; Han, X. Optimization scheduling control strategy of wind–hydrogen system considering hydrogen production efficiency. *J. Energy Storage* **2022**, *47*, 103609. [CrossRef]
22. Aubras, F.; Deseure, J.; Kadjo, J.J.A.; Dedigama, I.; Majasan, J.; Grondin-Perez, B.; Chabriat, J.P.; Brett, D.J.L. Two-dimensional model of low-pressure PEM electrolyser: Two-phase flow regime, electrochemical modelling and experimental validation. *Int. J. Hydrogen Energy* **2017**, *42*, 26203–26216. [CrossRef]
23. Lu, X.; Du, B.; Zhou, S.; Zhu, W.; Li, Y.; Yang, Y.; Xie, C.; Zhao, B.; Zhang, L.; Song, J.; et al. Optimization of power allocation for wind–Hydrogen system multi-stack PEM water electrolyzer considering degradation conditions. *Int. J. Hydrogen Energy* **2023**, *48*, 5850–5872. [CrossRef]
24. Honsho, Y.; Nagayama, M.; Matsuda, J.; Ito, K.; Sasaki, K.; Hayashi, A. Durability of PEM water electrolyzer against wind power voltage fluctuation. *J. Power Sources* **2023**, *564*, 232826. [CrossRef]
25. Crespi, E.; Guandalini, G.; Mastropasqua, L.; Campanari, S.; Brouwer, J. Experimental and theoretical evaluation of a 60 kW PEM electrolysis system for flexible dynamic operation. *Energy Convers. Manag.* **2023**, *277*, 116622. [CrossRef]
26. Gu, J.; Guo, B.; Hu, S.; Ding, S.; Zhang, T.; Tian, Z.; Yang, F.; Ouyang, M. Experimental studies on dynamic performance of a 250 kW alkaline electrolytic system. *J. Power Sources* **2024**, *592*, 233920. [CrossRef]
27. Zhang, Y.; Wang, X.; Nie, G.; He, C.; Yang, Y.; He, M.; Meng, X. Robust dispatch of multi-electrolyzer systems for renewable energy hydrogen production under wind forecast uncertainty. *Appl. Energy* **2026**, *409*, 127483. [CrossRef]
28. Guo, F.; Li, Y.; Shi, H.; Qu, J.; Tan, W. Optimization of power distribution for multi-stack electrolyzers system considering hydrogen production and voltage degradation. *Int. J. Hydrogen Energy* **2025**, *175*, 151452. [CrossRef]
29. Zhou, Z.; Zheng, M.; Dong, B.; Li, J. Cluster allocation strategy of multi-electrolyzers in wind-hydrogen system considering electrolyzer degradation under fluctuating operating conditions. *Renew. Energy* **2025**, *242*, 122381. [CrossRef]
30. Cheng, K.; He, S.; Hu, B. Power adaptive control strategy for multi-stack PEM photovoltaic hydrogen systems considering electrolysis unit efficiency and hydrogen production rate. *Sustain. Energy Technol. Assess.* **2025**, *75*, 104200. [CrossRef]
31. Zheng, W.; Lv, B.; Shao, Z.; Zhang, B.; Liu, Z.; Sun, J.; Yuan, J.; Jiang, C. Optimization of power allocation for the multi-stack PEMEC system considering energy efficiency and degradation. *Int. J. Hydrogen Energy* **2024**, *53*, 1210–1225. [CrossRef]
32. Zou, P.; Lin, H.; Zhou, X.; Zou, Y.; Li, Y.; Yan, G.; Duan, X.; Cai, J. Control strategies for multi-electrolyzer alkaline hydrogen generation systems improving renewable energy utilization and electrolyzer lifespan. *Renew. Energy* **2025**, *253*, 123628. [CrossRef]
33. He, H.; Xia, Y.; Li, L.; Feng, Q.; Wei, W. Adaptive power coordination control for electrolysis hydrogen directly driven by wind turbines. *IEEE Trans. Power Electron.* **2024**, *40*, 2315–2326. [CrossRef]

Disclaimer/Publisher's Note: The statements, opinions and data contained in all publications are solely those of the individual author(s) and contributor(s) and not of MDPI and/or the editor(s). MDPI and/or the editor(s) disclaim responsibility for any injury to people or property resulting from any ideas, methods, instructions or products referred to in the content.